Development of a Diffraction-Grating-Based Micro-Gravimetric Sensing Method for Biological Applications

by

Alibey Öztürk

A Thesis Submitted to the

Graduate School of Engineering

in Partial Fulfillment of the Requirements for

the Degree of

Master of Science

in

Materials Science & Engineering

Koc University

August 2008

Koc University

Graduate School of Sciences and Engineering

This is to certify that I have examined this copy of a master's thesis by

Alibey Öztürk

and have found that it is complete and satisfactory in all respects,
and that any and all revisions required by the final
examining committee have been made.

Committee Members:

_____
B. Erdem Alaca, Ph. D. (Advisor)

_____
Hakan Ürey, Ph. D.

_____
İ Halil Kavaklı, Ph. D.

Date: <u>4 July 2008</u>

ABSTRACT

A micromechanical system is developed utilizing a diffraction grating for high-precision displacement measurements. The device is in the form of released cantilevers and bridges made of Ni suspended over a Si surface. Hence, an operational diffraction grating is obtained. The structures are actuated in their resonant mode through magnetic means. A photodetector setup is built to track changes in the resonance behavior. The quality of the setup is evaluated using a well-calibrated sputtering system and applicability of the device to biosensing is demonstrated with human opioid receptors.

ÖZET

Yüksek hassasiyetteki deplasman ölçümleri için, kırınım ızgaraları kullanılan mikro-mekanik bir sistem geliştirildi. Aygıt, Si yüzey üzerinde serbest bırakılmış nikel çubuk ve köprülerden oluşturuldu. Bu şekilde, işlevsel bir kırınım ızgarası eldi edildi. Yapılar, manyetik bir şekilde çınlanım modlarında uyarıldı. Aygıtların çınlanım devranışlarındaki değişimi takip etmek için bir foto-dedektör düzeneği kuruldu. İyi kalibre edilmiş bir saçtırma sistemi ile düzeneğin kalitesi test edildi ve aygıtın biyolojik molekülleri algılaması, insan almaç proteinleri kullanılarak kanıtlandı.

ACKNOWLEDGEMENTS

I have completed this study under the supervision of Professor Erdem Alaca. He has continuously and kindly paid attention to my studies throughout my academic life in Koç University. I also thank to our collaborators Professor Hakan Ürey and Halil Kavaklı for their assistance along this thesis. We have carried out most parts of this project with İlker Ocaklı and I am grateful to him for that we have succedeed in this project together. Salih Kılıç and Natali Özber were the other members of this project on which we have worked together peacefully. Most important part of this thesis includes the photodedector setup that I have built in the Optical MEMs Laboratory and I thank to all the laboratory members, especially to Fatih Toy and Hüseyin Seren for their important help during the development of the optical system. I appreciate very much all the support of all our group members to my study, especially to Can Uslu who carried out the computational part of this project.

This thesis is completed under the support and endless love of my family and my future wife Pınar Kahraman. I am very happy for their presence in my life.

TABLE OF CONTENTS

LIST OF TABLES

LIST OF FIGURES

x

NOMENCLATURE

d	Spacing between the gratings
α	Diffraction angle
λ	Wavelength
δ	Optical path difference
I	Intensity
φ	Phase Shift
a	Grating Period
n	Number of the illuminated periods
σ	stress on the cantilever
E	Young's modulus
R	radius of curvature of the bended cantilever
v	Poisson's ratio
h	cantilever deflection
t	thickness of the cantilever
l	length of the cantilever
w	width of the cantilever
f_0	resonance frequency
k	stiffness
m	mass
n	coefficient that determines effective mass
ρ	density
f'	shifted resonance frequency
$\Re$	responsivity
ω_0	resonant angular frequency
Q	quality factor

A,D	oscillation amplitude
T	temperature
x	displacement
t	time

Chapter 1

INTRODUCTION

Ascendant demand for methods of detecting biological or chemical species raised a great interest in micro and nano-electro-mechanical systems (MEMS-NEMS) [1-3]. It is possible to fabricate inexpensive, prompt, and extremely sensitive mass-sensors with the new fabrication techniques offered [4-5]. Several techniques for the investigation of biochemical sensing applications such as detection of chemical analysts, viruses, cells, bacteria or DNA molecules have been reported [6-11]. In these approaches, adsorption of entities of interest is monitored via various detection mechanisms such as optical, electrical or mechanical readouts. It is possible to perform very fine mass measurements based on micro and nano-mechanical devices called cantilevers. Miniaturization of mass sensors leads to higher mass sensitivity and greater compactness which improves the functionality of the device. They can be used as force transducers when a force is applied on them by a small quantity of mass deposited onto the mechanical structure. Their dynamic and static responses to this additional mass can be measured in order to determine the quantity of the additional mass with spatial resolution. Piezo, magnetic, electrostatic, thermal and noise dependent methods are various techniques that are used for actuation of the devices [12-15]. Various transduction methods are reported including piezoresistive, capacitive, optical, interferometric and tunneling based approaches [16-19]. Cantilevers are inexpensive and reproducible devices that can be fabricated in batch using silicon micromachining techniques. They can also be combined with CMOS technology to increase both the functionality and sensitivity of the sensor by allowing it to operate in viscous media. Two

main operation modes are utilized to use cantilever transducers as mass sensors. Static mode of operation relies on the relation between the stress on the cantilever and the deflection caused by the loaded extra mass. Hence, amount of the loaded extra mass can be extracted by measuring the deflection of the beam [11]. Dynamic mode of operation depends on the measurement of the shift in the resonance frequency of the beam due to extra mass. Cantilevers can be driven at their resonance modes by magnetic actuation. Magnetic actuation eliminates the drawbacks such as charging, stiction due to small gaps and other limitations associated with the electrostatic method and also enables operation in liquid media.

In this study, dynamic transduction principle mentioned above is utilized with an integrated optical readout by means of magnetically actuated cantilevers. A photodiode (PD) circuit utilizing diffraction grating is used for this purpose.

Chapter 2 provides the background information regarding the operation principles and the optical readout. Diffraction grating is discussed in details. Static and dynamic modes of operations are reviewed afterwards.

Fabrication Flow and the Layout Design are explained in Chapter 3. Principles of the patterning method are reviewed briefly. Fabrication of the structures including patterning, electroplating and etching steps are provided.

Chapter 4 discusses the details of the experimental setup and procedure. Actuation and PD setups are described and verification of the measurements is demonstrated. Subsequent to verifications, characterization results of the cantilevers are provided and the results are discussed qualitatively.

Two case studies utilizing the cantilevers as mass sensors are provided in Chapter 5. Both the organic and inorganic mass sensing properties and the potential utilization of the devices as biosensors are demonstrated.

Discussion regarding the operation of the devices is given in Chapter 6. Stress accumulated onto structures via electroplating step and the results of the operation in liquid media are discussed. Remarks concerning PD output are emphasized and Finite Element Numerical Analysis results are provided.

The thesis is concluded with a short summary of the performed study and future research work.

Chapter 2

Operation and Optical Readout Principles

2.1 Diffraction Gratings

Collection of reflecting (or transmitting) elements separated by a distance comparable to the wavelength of light under study is called a diffraction grating. It may be thought of as a collection of diffracting elements, or a collection of reflecting grooves on a substrate. A reflection grating consists of a grating superimposed on a reflective surface, whereas a transmission grating consists of a grating superimposed on a transparent surface [20]. Gratings are of particular interest to scientists and engineers. When the period of a grating is comparable to the wavelength of the incident light, a physical phenomenon called diffraction is observed. Interaction of the incident beam with the periodic structure gives rise to multiple output beams, the so-called orders of diffraction. The angles of the diffracted orders vary as a function of the wavelength of the incident light. If the incoming light is multicolored, i.e., consists of more than one wavelength, then the angles of diffraction differ from one particular color to the next, resulting in a so-called spectrum of the incoming light [21].

When monochromatic light is incident on a grating surface, it is diffracted into discrete directions. Each grating groove can be pictured as being a very small, slit-shaped source of diffracted light. The light diffracted by each groove combines to form a diffracted wavefront. The usefulness of a grating depends on the fact that there exists a unique set of discrete angles along which, for a given spacing d between grooves, the diffracted light

from each facet is in phase with the light diffracted from any other facet, so they combine constructively [22]. Figure 2.1 shows schematic representation of diffraction orders.
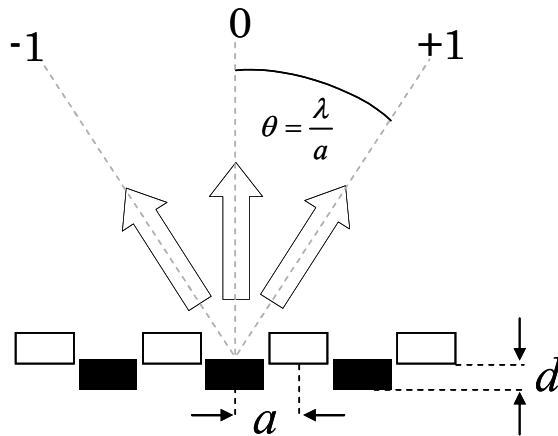
Figure 2.1: Schematic representation of diffraction orders. θ is the diffraction angle and λ is the wavelength of the light source [23].

.

When a light beam is focused on a grating, wavefront is separated such that one half of it is reflected from the fixed surface and one half by the movable fringes. Distance d between the two surfaces determines the optical path difference (OPD) δ between the two separate parts of the wave. Figure 2.2 shows the schematic representation of reflection of the light from a grating surface.
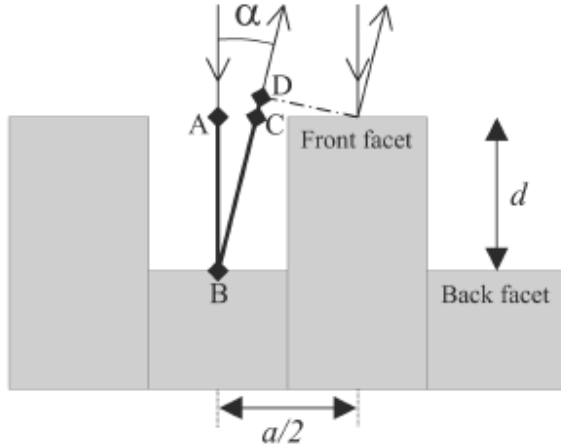
Figure 2.2: Schematic of the grating. Bold line represents the OPD δ between the reflected beams. δ is a function of diffraction angle, α and depth *d* of the grating. It's the sum of the distances AB BC and CD [24].

Intensity *I* of the diffraction pattern is given by:

$$I \propto \underbrace{\left(\frac{SinK}{K}\right)^2}_{I_1} \underbrace{\left(\frac{Sin2nK}{Sin2K}\right)^2}_{I_2} \underbrace{\cos^2\left(\frac{\varphi}{2}\right)}_{I_3} \tag{2.1}$$

where $K = (\pi a / 2\lambda)\sin\alpha$, *n* is the number of the illuminated periods, *a* is the grating period and α is the diffraction angle. Phase shift $\varphi = (2\pi / \lambda)\delta$ is determined by OPD δ, which is the sum of the distances AB BC and CD in Figure 2.2 [25]:

$$\delta = d\left(1 + \cos\alpha + \frac{a}{2d}\sin\alpha\right) \tag{2.2}$$

In equation 2.1, intensity I has three contributions. I_1 is a sinc function resulting due to rectangular shape of the gratings. The width of the I_1 is inversely proportional to the period of the gratings since it is the square of the Fourier transform of the grating shape. I_2 is a comb function due to periodicity of the grating. Angular separation between the peaks is determined by the grating period and the width of the each peak is determined by the number of illuminated fingers. I_3 determines the phase shift due to gap between the gratings and the fixed surface [26]. These contributions are illustrated in Figure 2.3 for a phase shift corresponding to $\varphi = N2\pi$ and $\varphi = \pi + N2\pi$ (N is an integer). OPD $\delta = 2\pi$ for the zeroth order diffraction since $\alpha = 0$ and intensity I modulates like as a cosine function of the OPD.
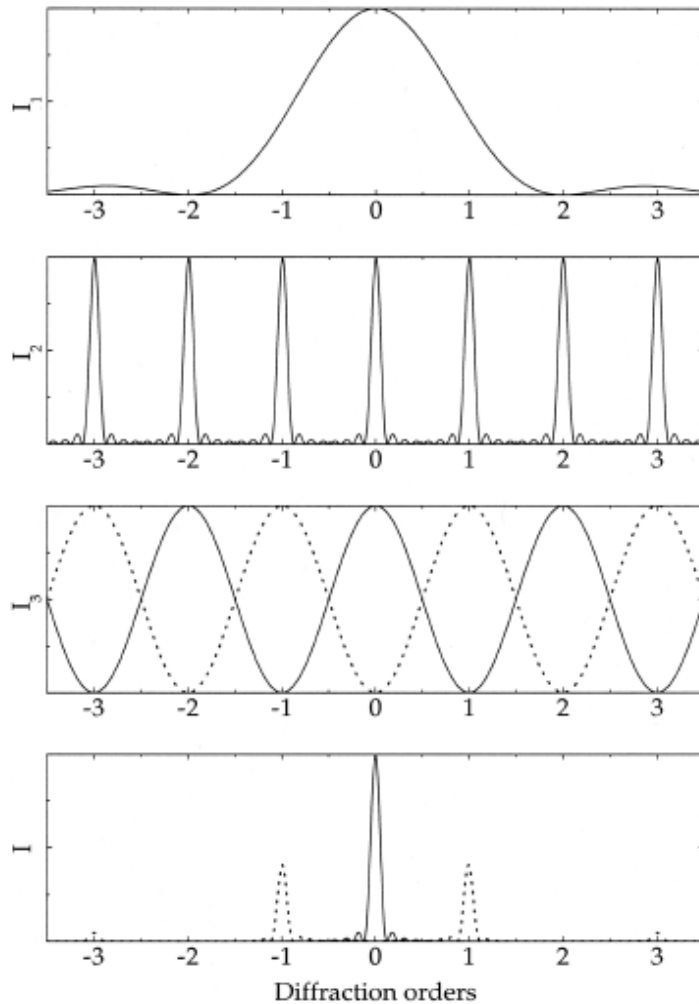
Figure 2.3: Intensity I of the diffraction pattern of a grating. I is the multiplication of I_1, I_2 and I_3. Solid curve represent a phase shift of $\varphi = N2\pi$ and dotted curve represents $\varphi = \pi + N2\pi$ [25].

If the gap between the movable and the fixed surfaces is an integer multiple of $\lambda/2$, equation 2.2 states that the OPD δ becomes λn for the zeroth order diffraction (n is an integer). Then the phase shift $(2\pi / \lambda)\delta = 2\pi n$ provides the intensity maxima due to

equation 2.1 . If the gap is an integer multiple of $3\lambda/4$, OPD δ becomes $3\lambda/2$ and phase shift, $(2\pi/\lambda)\delta = \varphi = \pi + N2\pi$ and the intensity minima occurs with respect to the gap. Hence, intensity I changes with a period of $\lambda/2$. This behavior is shown in Figure 2.4:
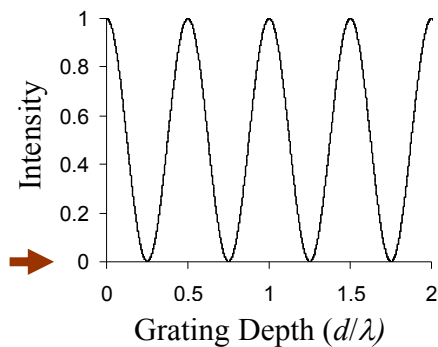
Figure 2.4: Intensity changes with a period of $\lambda/2$

Utilizing the intensity modulation of the diffraction orders, deflection of a moving structure can be calculated. In this study, frequency response of a cantilever is determined by observing the maximum intensity modulation since the deflection of the cantilever will be maximum at resonance. [28-29]. Fabrication of the gratings will be explained in Chapter 3.

2.2 Mass Detection Methods

Two main methods have been studied in literature for mass detection by means of micro-cantilevers. First one, so called static mode of operation, utilizes the measurement of the bending of the cantilever due to stress caused by extra mass loading. Second one, so called dynamic mode of operation, utilizes the measurement of the shift in the resonance

frequency of the cantilever caused by the extra mass. The relation between the bending of a cantilever beam and the stress is given by equation 2.3 [30]:

$$\Delta h = \frac{3l^2(1-\upsilon)}{Et^2}\sigma \qquad (2.3)$$

where Δh is the bending of the cantilever, l is the length of the cantilever, v is the Poisson's ratio, E is the Young's Modulus, t is the thickness of the beam and σ *is the* stress. Hence, measuring the bending of the cantilever due to stress, loaded extra mass can be extracted.

Dynamic mode of operation utilizes the dynamic response of the cantilever due to the accreted species. If a cantilever is driven in its resonance frequency, there will be a shift in the frequency when an extra mass is loaded to the beam. Amount of the shift of the resonance frequency is related directly to the amount of the loaded mass. Resonance frequency of a cantilever beam is given by equation 2.4:

$$f_0 = \frac{1}{2\pi}\sqrt{\frac{k}{m*}} \qquad (2.4)$$

Where k is the stiffness of the beam and defined as:

$$k = \frac{Et^3w}{4l^3} \qquad (2.5)$$

And m^* is the effective mass and defined as:

$$m* = n(\rho wlt) \qquad (2.6)$$

In above formulas, w is the width, l is the length, t is the thickness and ρ is the density of the beam. n is a geometry dependent constant ($1>n>0$). For one end fixed cantilevers, it is

defined to be 0.24 [31]. Combining equations (2.4), (2.5) and (2.6), resonance frequency of a one end fixed cantilever can be expressed as:

$$f_0 = \frac{1}{2\pi} \frac{t}{l^2} \sqrt{\frac{E}{\rho}} \qquad (2.7)$$

Oscillation amplitude of the cantilever is maximized at resonance frequency. If an extra mass, Δm is loaded on the cantilever, new resonance frequency can be defined as:

$$f_0' = \frac{1}{2\pi} \sqrt{\frac{k}{m* + \Delta m*}} \qquad (2.8)$$

In equation 2.8, $\Delta m^* = \Delta m$ if the mass is attached only to the end of the cantilever and $\Delta m^* = 0.24\Delta m$ if the mass is distributed properly onto the surface of the cantilever beam. If it is assumed that the stiffness of the cantilever does not change after mass loading, Δm can be extracted as [32]:

$$\Delta m = \frac{k}{4\pi^2} \left(\frac{1}{f'^2} - \frac{1}{f_0^2} \right) \qquad (2.9)$$

Sensitivity of a cantilever sensor is mostly defined as [32-33]:

$$\delta M \approx \Re^{-1} \delta\omega_0 \qquad (2.10)$$

Here, $\delta\omega_0$ is the minimum detectable frequency shift, δM is the minimum detectable mass and $\Re$ is the *mass responsivity* of the device which is given in equation 2.11

$$\Re = \frac{\partial \omega_0}{\partial M_{eff}} = \frac{-\omega_0}{2M_{eff}} \qquad (2.11)$$

Equations 2.10 and 2.11 suggest that the minimum detectable mass is determined by the intrinsic properties of the cantilever beam and the minimum detectable frequency shift. As equations 2.10 and 2.11 state, minimum detectable mass is dependent on the resonance frequency of the structure. Minimum detectable mass decreases as the resonance frequency of the beam increases. Hence, higher sensitivity's can be achieved by devices which resonate at higher frequencies. Equation 2.7 suggests that resonance frequency of a structure is inversely proportional to square of its length. This is the main motivation behind the miniaturization of the devices.

Chapter 3

LAYOUT DESIGN and FABRICATION FLOW

3.1 Introduction

Fabrication of micro-structures starts with a fundamental process called photolithography. Photolithography is a patterning method which creates the image of a mask onto the substrate surface which is covered by a photo-resist layer. Photoresist is an imagable liquid film that can be spread out onto a substrate. Then it can be patterned by photolithography and developed into a selectively placed layer for further processing.

UV lithography is the most commonly used lithography technique. During the process, UV light is shined through a mask onto the substrate which is covered by photoresist. The mask stops some of the light from proceeding onto the substrate surface. Then, the light beams that passes the mask exposure the surface to transfer the geometry on the mask to the substrate. If the photoresist is positive, sections which are not exposed by UV light remains after the development. If it is negative, then the sections exposed by UV light remains. Figure 3.1 shows the patterning process [33].
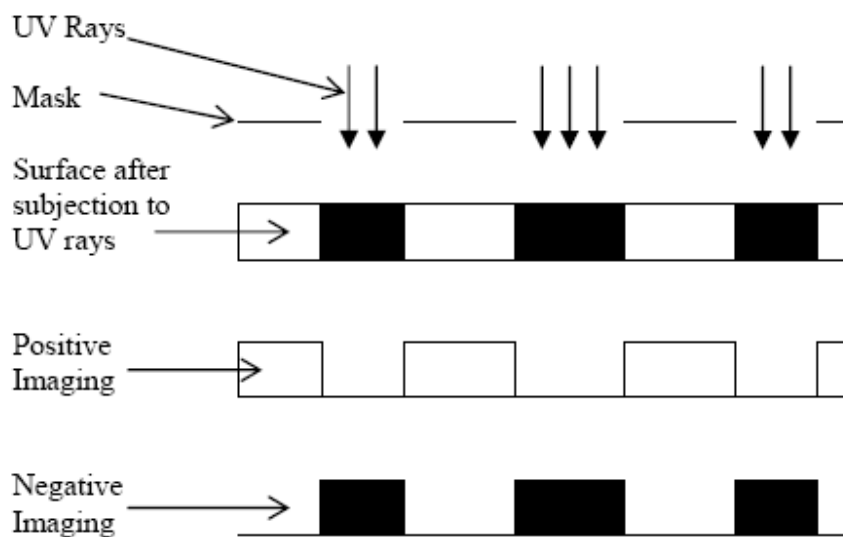
Figure 3.1: Patterning diagram [33]

3.2 Layout Design

UV photolithography explained above is used in the fabrication of micro-resonators. Diffraction gratings are embedded onto the structures for the optical readout. A photolithography mask is designed for patterning of the structures on a <100> 4" single-crystal silicon wafer. The mask is designed to include cantilevers of various sizes. The mask is composed of individual dices in which the width of the cantilevers are kept constant. Width of the cantilevers varies from 2 μm to 12 μm. Length to width ratios are specified as 5, 10, 15 and 20. Cantilevers are designed to have diffraction grating platforms having 2, 3, and 5 µm of grating size and 3 and 4 periods. Gratings are tilted with respect to the long axis of the cantilever for the optical readout purposes. Cantilevers are attached to

anchors which have 100 μm widths. 4 contact points are included in each die to reduce the thickness variation during the electroplating.

Mask is designed with a layout editor. Anchors are aligned 45° with respect to the major axes of the wafer to ease releasing of cantilevers in of etching process. Each die is divided into several arrays in which specific types of cantilevers are included. Guide numbers are added to each array to recognize the size of the cantilevers. The image of the layout is show in Figure 3.2.
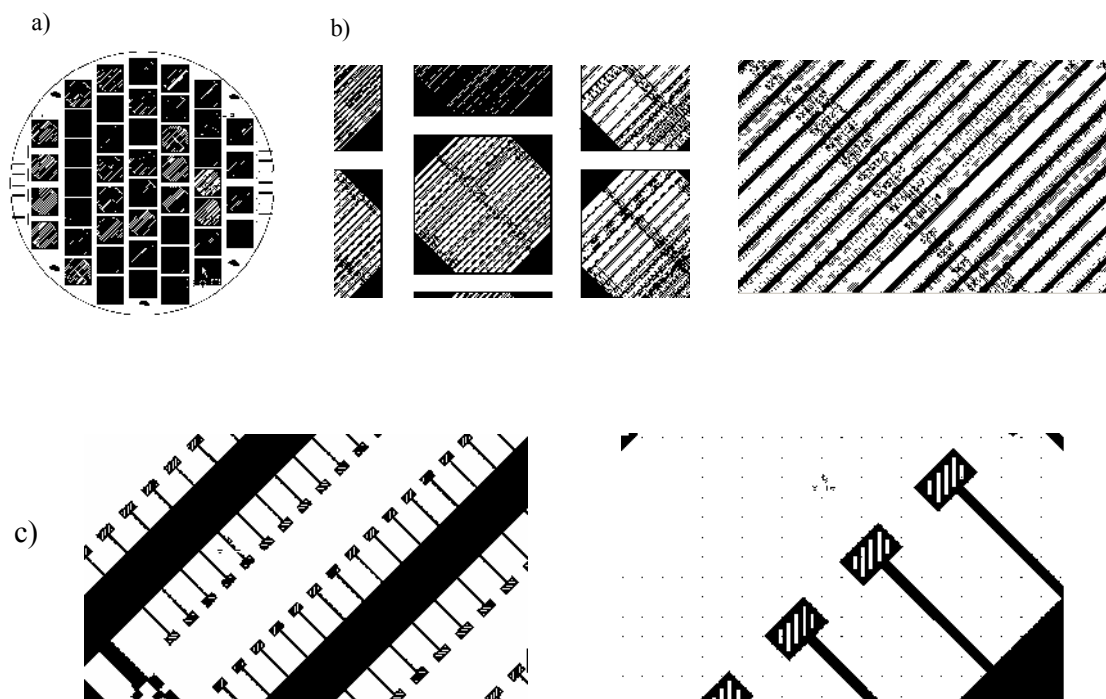
Figure 3.2: image of the layout through 5 zoom steps.

Subsequent to its design, the layout is transferred on a photolithography mask by means of a commercial company.

3.3 Fabrication Flow

Fabrication is carried out on a 4" single-crystal silicon wafer with a thickness of 525±25 μm and a resistivity of $0.1 - 0.5$ Ω·cm. Prior to the fabrication flow, a 10nm/100nm Cr/Au layer is sputtered onto the Si after standard cleaning of the wafer. Au layer serves as the seed layer for the subsequent electroplating step and also it is necessary for the functionalization of the structure for binding of the bio-molecules. Cr layer ensures the adhesion between the Au and Si layers. Schematic representations of sputtered layers are shown in Figure 3.3.
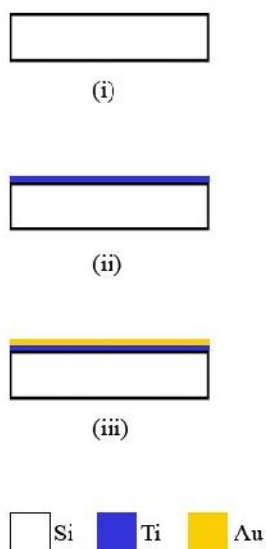
Figure 3.3: Sputtering of the seed layers onto the Silicon wafer

Chapter 3: Layout Design and Fabrication Flow

Fabrication of the structures implies three main steps: Patterning of Au, Nickel electroplating and releasing the cantilevers by etching. Each step is studied gingerly and will be explained in following subsections.

3.3.1 Patterning of Au

UV photolithography is used for the patterning of the gold surface as mentioned in previous sections. Prior to lithography, wafer is covered by the photoresist by a spinner. PR AZ 5214E photoresist is used. Spinning parameters are important to achieve the desired PR thickness. Parameters are adjusted to obtain 2μm thickness of PR since the desired thickness for the cantilevers are around 1μm. 3000 rpm for 20 s + 5000 rpm for 30 seconds (Figure 3.4) are calculated for approximately 2μm coating of PR. Then, PR is soft-baked for 10 minutes at 108° on the hot plate without cover to drive off excess solvent. Duration of the UV exposure is adjusted to obtain the maximum resolution. Duration time of UV is so sensitive that even 0.5 seconds of more or less exposure changes the obtainable minimum feature size. Specifically, PR on the gratings should be preserved during the exposure since they would not be electroplated. Three to five seconds of exposure is carried out for this purpose and minimum feature size of 3μm is obtained. Image of the Au layer after exposure is shown in Figure 3.5
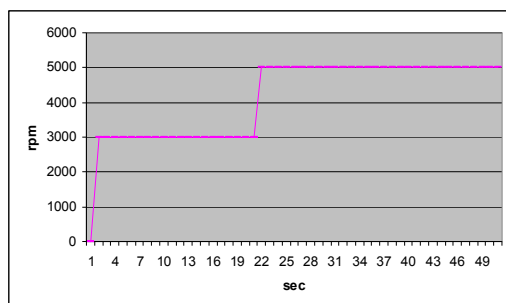
Figure 3.4: Spinner parameters for PR coating

a)

b)

c)
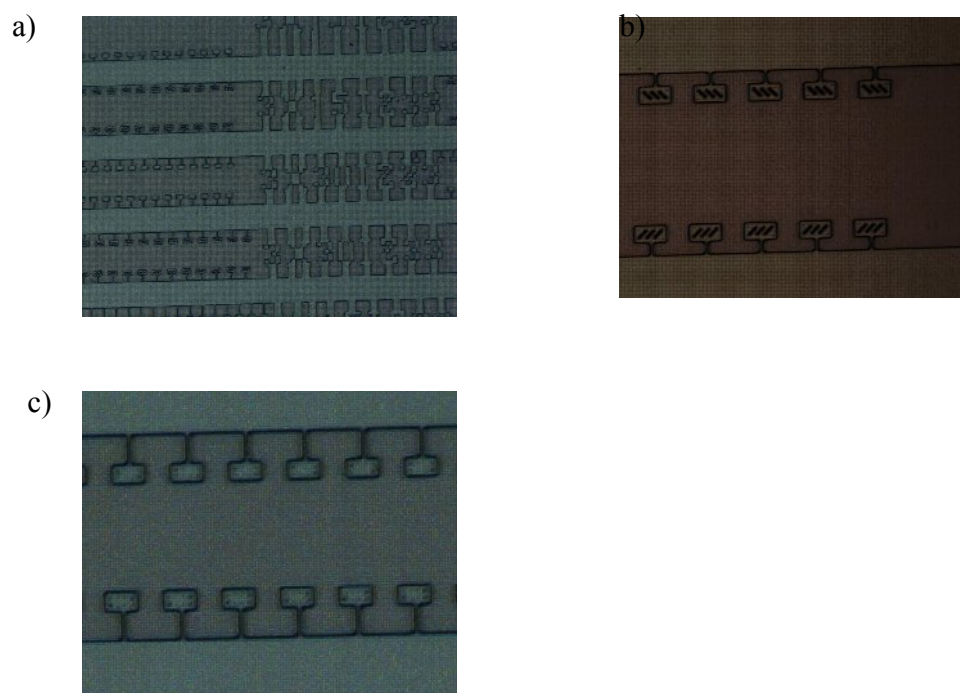
Figure 3.5: a) Image of the cantilevers after UV exposure.

b) Cantilevers having grating size of 3μm

c) Cantilevers having grating size of 2 μm

Width of the cantilevers is 3µm, lengths are 15µm and grating sizes are 2 or 3µm in Figure 3.5. As it is seen in the last micrograph, resolution for the 2µm gratings could not be obtained even though many trials regarding the exposure time is carried out. The minimum feature size is mainly determined by the resolution limit of the aligner. Subsequent to the UV exposure, wafer is developed in 1:5 or 1:4 "AZ 4400© Developer" and DI water for 30 seconds to 2 minutes depending on the deformation on the exposed parts of the PR. The schematic view of the exposure and development procedure is shown in Figure 3.6.
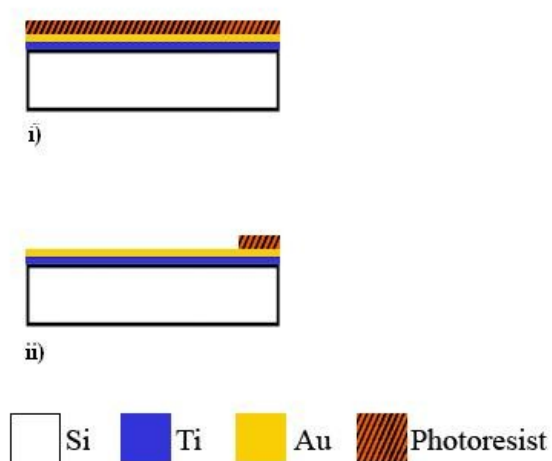
Fig 3.6: i) Spin coating of the photoresist

ii) Developed structure after UV lithography

3.3.2 Electroplating of Nickel

After the lithography, the wafer is diced and cantilevers are obtained by electroplating of Ni on individual dice in a nickel sulphamate bath [34]. Bath is composed of 600 g/L Ni(SO$_3$NH$_2$)$_2$.4H$_2$O, 10 g/L NiCl$_2$.6H$_2$O and 40 g/L H$_3$BO$_3$. After the

electroplating, PR is stripped of with acetone and the main structures are obtained. Schematic view of the bath and the deposition is shown in Figure 3.7.

a)

b)
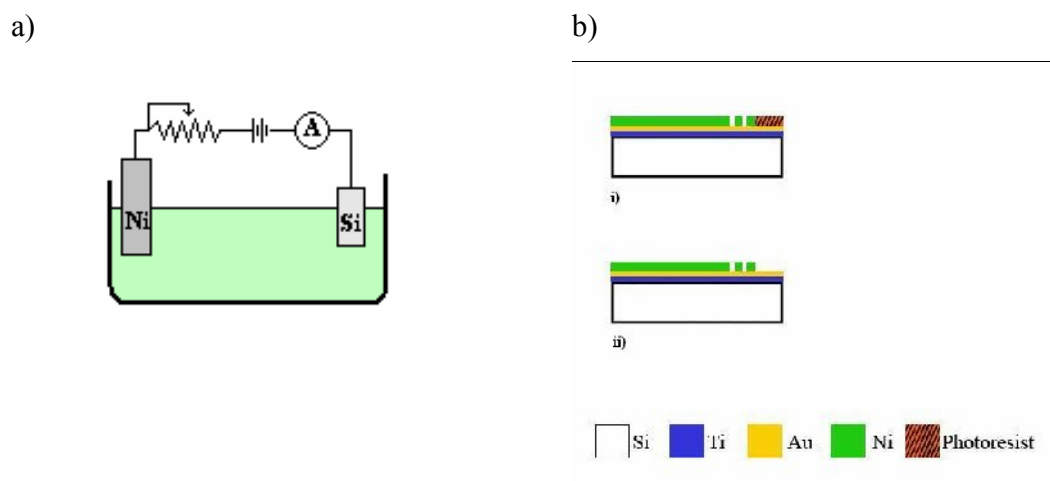
Figure 3.7: a) Schematic view of electroplating bath

b) electroplating and subsequent removal of the photoresist

The thickness and the roughness of the cantilevers are controlled by arranging the current density, duration of the deposition and temperature. Each of the four corners of the dice is used as the electrical contact and the bath is continuously stirred to establish a uniform deposition. The temperature is set to 40°C and current densities varying between 5 and 25 mA/cm^2 are used as studied in literature for a proper Ni electroplating [35]. Photoresist is stripped off with acetone following the formation of the cantilevers. Structures after electroplating are shown in Figure 3.7:

Chapter 3: Layout Design and Fabrication Flow
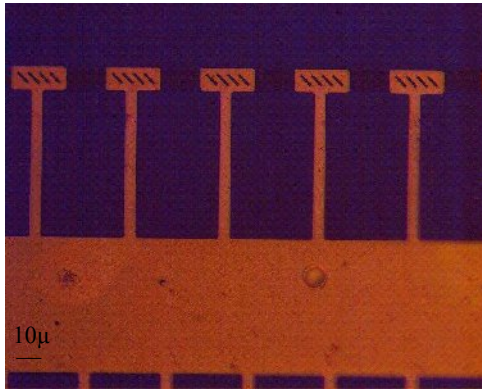
Figure 3.7: Ni deposited structures. PR is stripped off.

3.3.3 Releasing the Structures by Wet etching

In order to form a functional MEMS, it is necessary to etch the previously deposited layers beneath the device for release. Au and Cr layers under the electrodeposited Nickel are etched for this purpose. Au layer is etched just enough to reach the Si substrate and preserved underneath the cantilever for functionalization purposes. Afterward, the Silicon substrate is etched to release the structures and make them functional devices that oscillate above the Si surface connected to anchors formed by electroplating. Schematic representation of etching is shown in Figure 3.8.
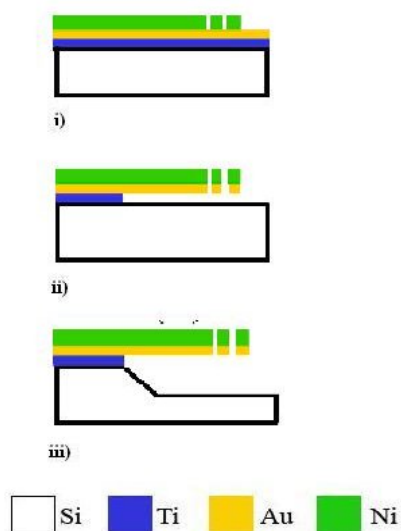
Figure 3.8: Cr, Au and Si etching respectively.

Au layer is etched in a commercial Gold Etchant TFA / GE-8148. Although the etchant does not attack nickel, it is observed seen that the device gets damaged when it is exposed to chemical etchants more than a few minutes. One minute of etching sufficed to etch 100 nm Au layer on the Silicon substrate. Gold layer under the cantilevers are kept during etching which will be utilized during the functionalization of the cantilevers for binding of proteins.

Cr layer is etched in a commercial Chromium Etchant TFE. Since the Cr layer is relatively thin, the etching is done nearly in 10 seconds. Main purpose of Au and Cr etching is to reach the Silicon surface where wet anisotropic etching will be carried out to realese the structures. Silicon surface is etched in a 35% KOH solution and the temperature is set to 75° during etching to minimize the surface roughness [36]. Ni served as a natural etch mask during this step eliminating the need for further lithography. Ni also imparts

corrosion resistance, a necessary feature for reliability in biosensor applications. Figure 3.9 shows an array of cantilevers that are ready for magnetic actuation.
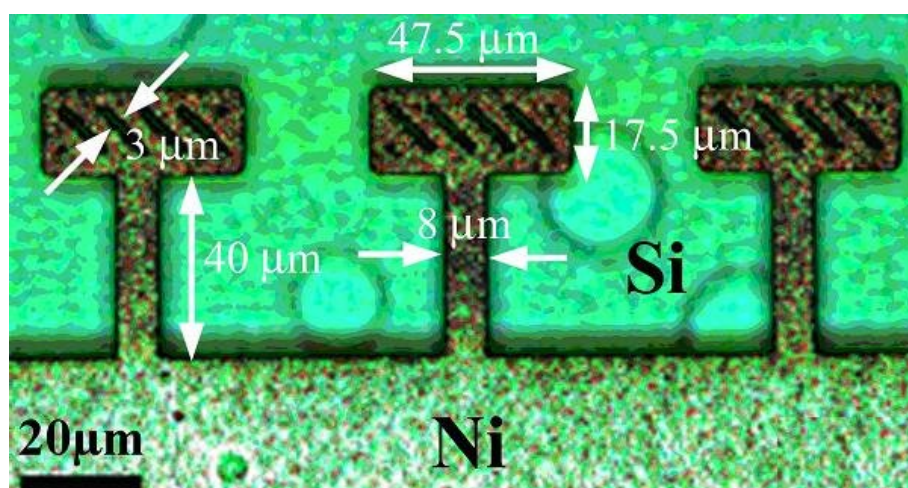
Figure 3.10: Released cantilevers which are ready for actuation.

The roughness of both the movable Ni surface and the fixed Si surface is evident in this micrograph.

Subsequent to fabrication of the cantilevers, the devices are operated as sensors for mass sensing applications. An integrated optical readout is used to characterize the devices and magnetic actuation is used to operate the devices at their resonance frequencies. Experimental setup and procedure will be explained in the next section.

Chapter 4

Experimental Setup and Procedure

4.1 Actuation Setup

Magnetic actuation is used to oscillate the devices at their resonance frequencies since the dynamic mode of operation is utilized for the fabricated micro-resonators. Actuation is carried out by means of an external magnetic coil with the prospect of being micromachined as a part of the process [37]. Magnetic actuation eliminates the drawbacks such as charging, stiction due to small gaps and other limitations associated with the electrostatic method and also enables operation in liquid media. Cantilevers are excited by a signal generator followed by a current amplifier. Sinusoidal signals are used to drive the cantilevers at their resonance modes. Schematic representation of the characterization setup is shown in Figure 4.1.
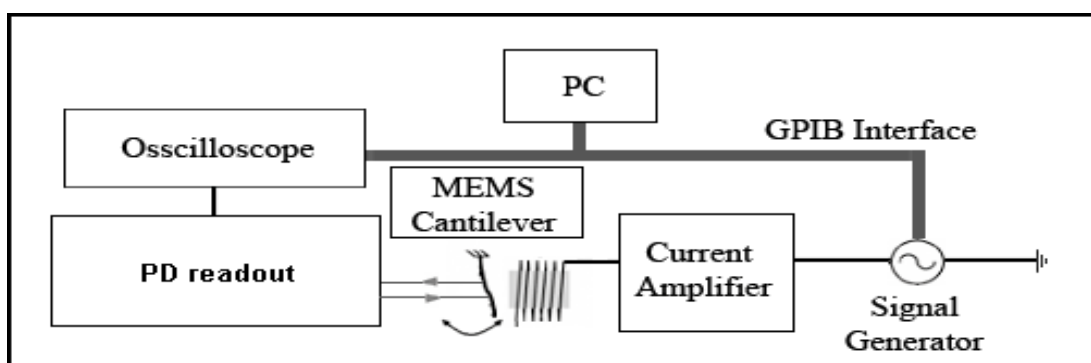
Figure 4.1: Characterization setup.

Chapter 4: Experimental Setup and Procedure

The input and output signals are monitored via an oscilloscope. In order to extract the frequency response and the resonance frequency of the beams, the driving signal is swept for a band of frequencies; and the PD output is recorded. The resonance frequency can be detected by recording the frequency where maximum peak-to-peak voltage is observed because maximum deflection occurs at the resonance frequency and this map the maximum peak to peak voltage readout of the photo diode circuit

4.2 Photo detector Setup

A Photo detector setup is built in order to utilize the grating interferometry. A photograph of the setup is shown in Figure 4.2.
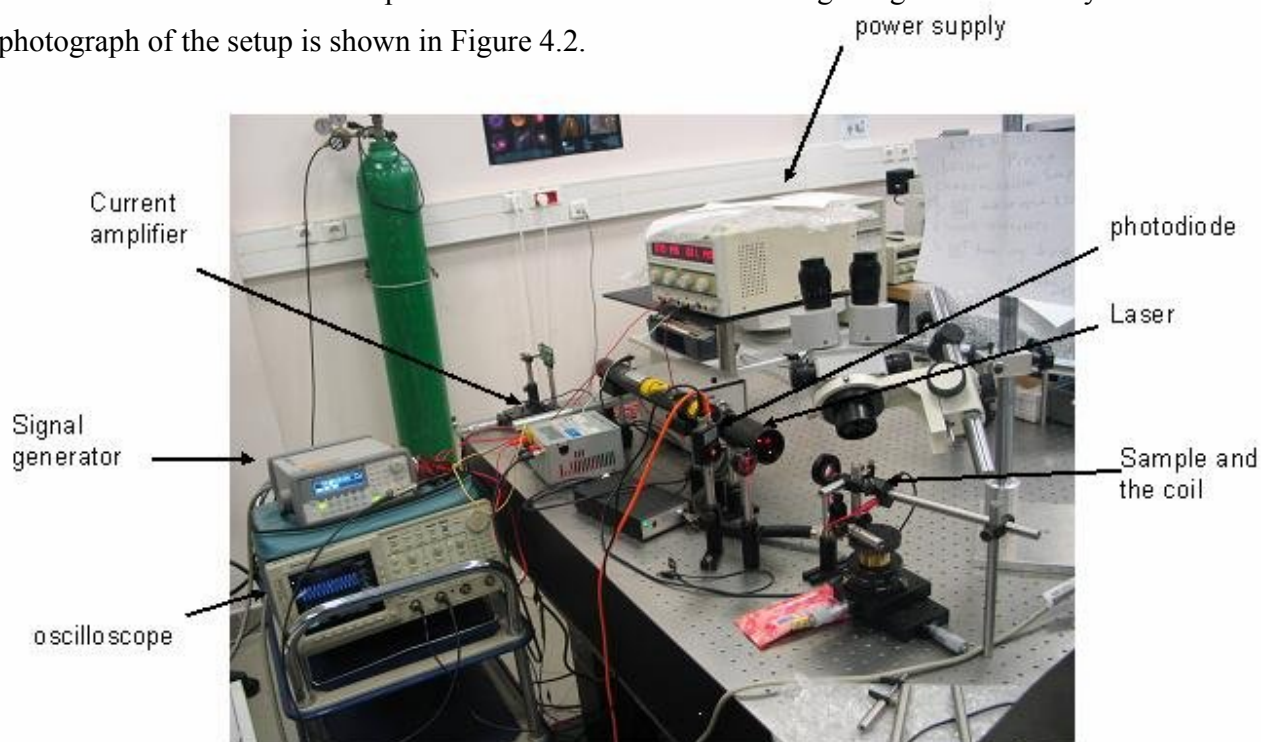
Figure 4.2: Photograph of the experimental setup

Principle of operation is depicted in Figure 4.3. A deflection of the cantilever causes modulation in the 0th and 1st orders of the diffracted light. The intensity changes periodically with the air gap between the cantilever and the substrate with a period of $\lambda/2$, where λ is the wavelength of the laser. Thus, the deflection can be measured by monitoring the sinusoidal intensity modulation. In order to extract the frequency response and the resonance frequency of the beams, the driving signal is swept over a band of frequencies and the PD output is recorded. The resonance frequency can be detected by recording the frequency where the maximum peak-to-peak voltage is observed [37,17,38]. Shot-noise limited detection can be achieved by monitoring both 0th and 1st order diffracted light to cancel laser and other noise sources [38].
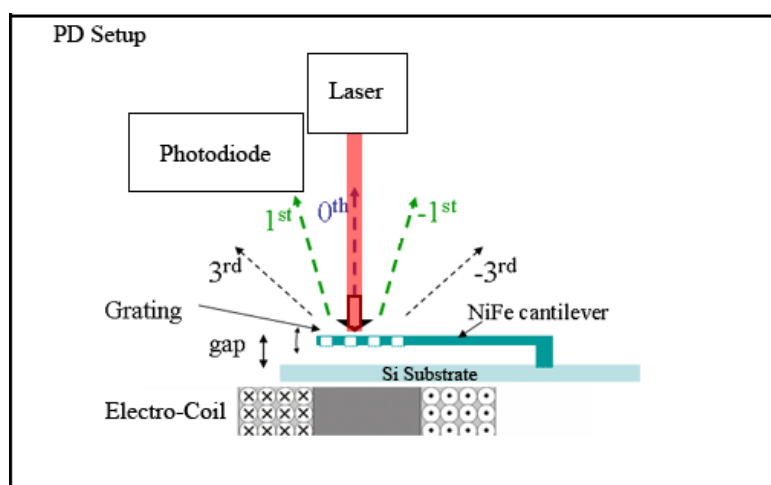
Figure 4.3: Optical readout and magnetic actuation principle. PD intensity is a sinusoidal function of the gap with a period of $\lambda/2$

Sample is illuminated by using a He-Ne laser with 633 nm wavelength. Then, 1st or 0th order diffraction of the light reflected from the gratings is focused on a wideband amplified Si photodiode. The photodiode output is monitored by the oscilloscope. Using

the GPIB interface and a computer program cantilevers are driven at a range of frequencies. Experimental flow is presented in Figure 4.4.
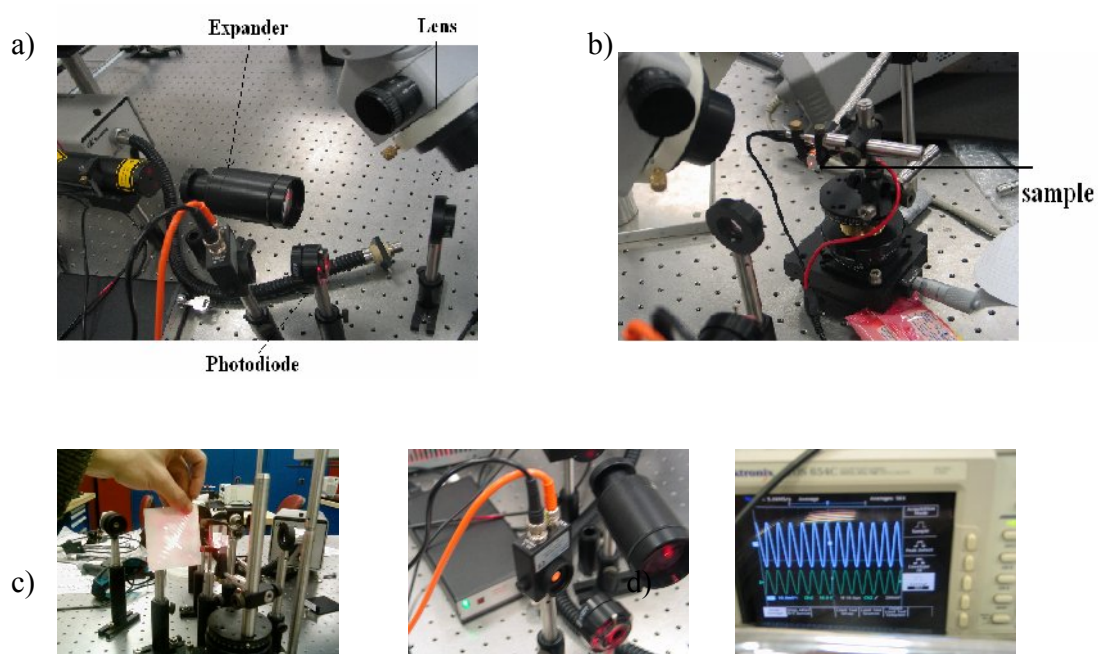
Figure 4.4: a) He-Ne Laser Source

      b) Illumination of the sample (Laser beam is focused on a grating platform of a single cantilever beam)

      c) Diffraction orders formed by the reflection of the light from the gratings

      d) Focusing the first order of the diffracted light onto the photodiode

      e) Sinosidal output signal at the driven frequency

Laser is focused onto the gratings by using the x-y-z stage under the sample. Intensity modulation of the 1st order diffracted light from the short cantilevers, which have

higher resonance frequencies and lower deflections, is found to be below 10 mV. At such low values, the noise became significant and to avoid it 0th order diffracted light is utilized which has a greater intensity than the 1st order.

4.3 Verification of the Measurements

The output signal explained above is utilized to extract the resonance frequency of the cantilevers. Maximum peak to peak voltages are recorded within the driven frequencies and the resonance behavior of the cantilevers is extracted from the intensity and phase modulations. Measurements done with the PD setup are compared against the readings of a Laser Doppler Vibrometer (Polytec OFV-2500 with a bandwidth of 0,5 Hz – 250 kHz). Those analog measurements are done on the same specific structures. The results of both LDV and PD measurements are found in complete agreement. Also, it is observed that the noise in the PD measurements are comparable to that of LDV with an RMS error of 1.5 Hz although no vibration isolation is used for the PD measurements. RMS error is the deviation of the phase data from the linear fit at the resonance transition. Linear fit to experimental data is shown in Figure 4.5
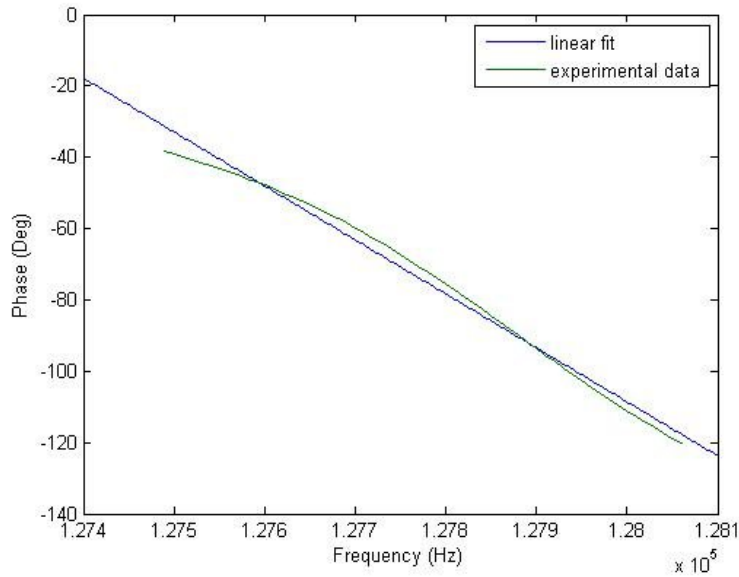
Figure 4.5: Linear fit approximation to experimental data

Then the RMS error is calculated using equation 4.1.

$$RMS = \sqrt{\frac{1}{N}\sum_{i=1}^{N}(x_i - \bar{x}_i)^2} \qquad (4.1)$$

where x_i is the actual data point and $\bar{x}_i$ is the corresponding linear fit data point. On the other hand, vibration isolation is needed for the LDV measurements to obtain a clear resonance curve. Comparison of the results of a specific structure is given in Figure 4.6.
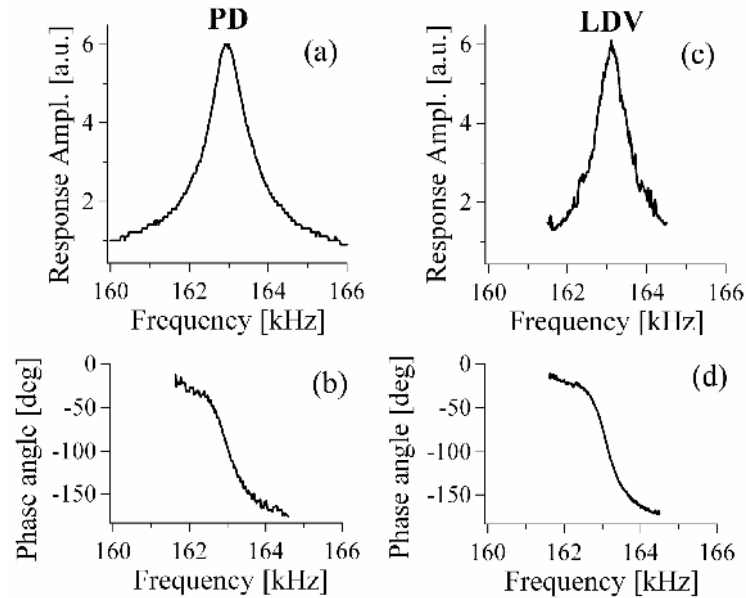
Figure 4.6: Comparison of LDV and PD measurements for a cantilever of 8 μm × 40 μm (a) PD resonance curve. (b) PD phase shift. c) LDV resonance curve. (d) LDV phase shift

As it is clearly seen in the figure 4.6, PD measurements extracts the resonance behavior of the cantilevers clearer than the LDV measurements does. Subsequent the comparison of the results of a single device, various experiments are done to verify the measurements by using cantilevers of various lengths. The thickness is kept constant at 0.7 μm and the width is 8 μm. The results of the comparison are given in Table 1.

Chapter 4: Experimental Setup and Procedure

Cantilever width × length	LDV resonance frequency (Hz)	PD resonance frequency (Hz)
8 µm × 40 µm	163110	162960
8 µm × 80 µm	64800	64770
8 µm × 120 µm	35390	35310
8 µm × 160 µm	17900	17900

Table 1: Comparison of the resonance frequencies of the cantilevers measured by PD and LDV setups.

The slight difference between the results of PD and LDV measurements provided in Table 1 is related to reading of the resonance curves. Especially LDV measurements are quite noisy so that the resonance frequency extracted from the resonance curve has a reading error.

After the verification of the measurements done with PD, cantilevers of various dimensions are characterized. The results will be provided in the next section.

4.4 Characterization of the Cantilevers

Different chips including various sizes of cantilevers are characterized after the verification of the measurements. Resonance behaviors and quality factors of almost 100 cantilevers on five different dies are observed. Dies including cantilevers types of which have width of 5, 6, 7, 8, and 11 µm are studied. Thickness is kept constant at 1.2 µm in all chips. Relation between the geometry of the cantilever and its resonance frequency is analyzed by using obtained data. Also the relation between the quality factors of the structures and resonance frequencies are studied.

4.3.1 Length Dependence of the Resonance Frequency

When the characterization data is analyzed, it is seen that the resonance frequencies and the quality factors of the cantilevers increase by decrease in their lengths. Variation of the resonance frequency regarding the change in length is given in Figure 4.7
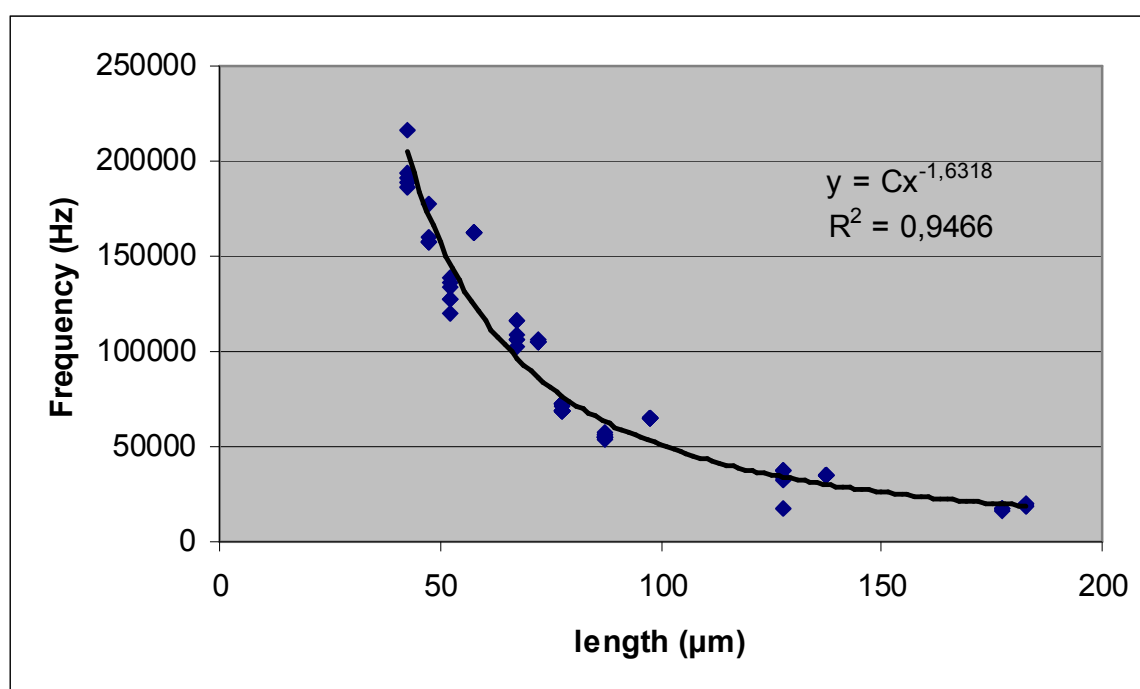
Figure 4.7: Resonance frequency distribution of the cantilevers

In Figure 4.7, resonance frequencies of some specific cantilevers are plotted. Filled dots represent the resonance frequencies of cantilevers and the solid line represents the is the fitted curve to data. R^2 value is called the proportion of the variability which shows the goodness of the fit to the data. Resonance frequency of a rectangular cantilever beam is inversely proportional to square of its length. On the other hand, when the length decreases,

Chapter 4: Experimental Setup and Procedure

the resonance frequency of the structures seem to decrease slower than the expected rate for a cantilever beam without grating platform.

4.3.2 Relation between the Resonance Frequency and Quality Factor of the Devices

Quality factors of cantilevers having different resonance frequencies are also studied. Relation between the resonance frequency and the Q factor is given in Figure 4.8
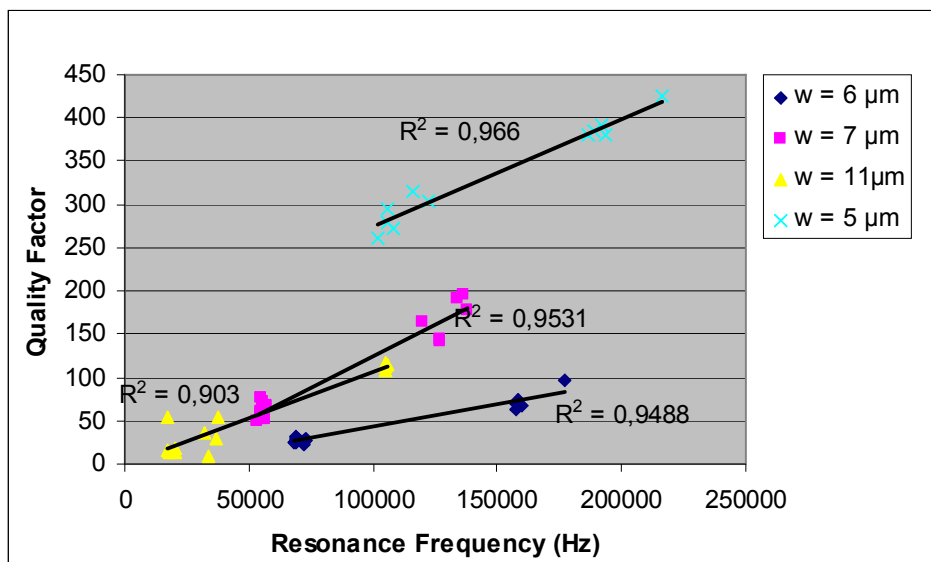
Figure 4.8: Quality factors of cantilevers having different resonance frequencies.

It is obvious in Figure 4.8 that Q factor of a structure increases with increasing resonance frequency. 4 different lines represent the behavior of the quality factors in 4 different chips in Figure 4.7. Increasing Q factor with increasing resonance frequency is the impact of the miniaturization of the device on the Q factor. It is stated in previous studies that the Q factor of a cantilever beam is also proportional t/L^2 where t and L is the

thickness and the length of the structure, respectively [39] . So, a linear relationship between the Q factor and the resonance frequency is expected and the behavior shown in Figure 4.8 reveals this behavior. Reason of the deviations from the linear behavior is that the thicknesses of the cantilevers do not have exactly the same value due to rough distribution during the electroplating setup. Since the resonance frequency of the structures is proportional to thickness, it is the parameter that disrupts the linear relation.

4.3.3 Thickness Dependence of the Resonance Frequency

To study the thickness dependence of the resonance frequency, three different chips are fabricated which include the cantilevers having the same geometry. Thicknesses of the chips kept different and by measuring the resonance frequency of the cantilevers of same geometry, thickness dependence is observed. Cantilevers having a width of 5 µm and length of 25 µm are characterized for this purpose. Thickness of the cantilevers on the same chip is averaged since there is a thickness variation even along a single cantilever. Results are shown in Figure 4.9.
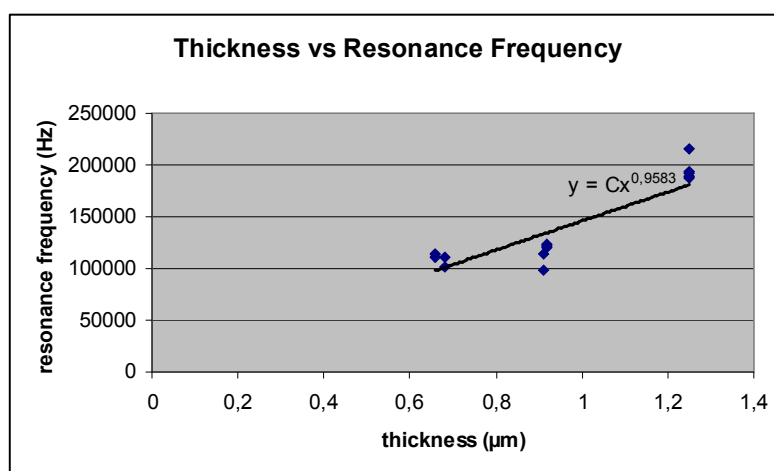
Figure 4.9: thickness dependence of the resonance frequency

Chapter 4: Experimental Setup and Procedure

Almost linear relation between the thickness and the resonance frequency is observed. Theoretically, thickness of cantilever, without grating platform, is expected to have a linear dependence on the resonance frequency. The same dependence is found to be valid for a cantilever having a grating platform.

To sum up the results of the characterization, the behavior expected for a cantilever beam found to be valid for a cantilever having a grating platform. Qualitatively, resonance frequency of a cantilever is proportional to inverse square of its length. Quality factor of the cantilever is proportional to its length and the resonance frequency has a linear relation with thickness of the cantilever.

After characterization of the cantilevers, the operation and the mass responsivity of the devices are studied via three different methods. Three case studies for the mass detection will be provided in the next section.

Chapter 5

Case Studies in Mass Detection

5.1 Overview

Resonance frequency of a cantilever has a linear relation with the loaded extra mass as explained in the first chapter ($\delta M \approx \Re^{-1} \delta \omega_0$). Three different case studies are done to observe this relation, find the resolution limit of the devices and to test the device for bio-sensing. In the first method, a well calibrated sputtering system is utilized to deposit known amounts of gold on the sensor and the associated shift in the resonance frequency is measured. Assuming the stiffness of the structures is unchanged after the mass loading, mass responsivity of the characterized specific device is found. A linear relation between the frequency shift and loaded extra mass is observed with a small deviation. The exact linear relation can be observed under the condition that the loaded extra mass is much smaller than the mass of the cantilever. The measurements are also validated by finite element numerical analysis which will be discussed in the last chapter. In the second and third method, the ultimate function of the device as a biosensor is tested. Protein molecules are attached to the cantilevers and the corresponding resonance frequency shifts are measured. Mass of the attached proteins is calculated by using FEM analysis and the reliability of the device is observed by comparing the theoretical expected mass of the attached proteins and result of the FEM analysis.

5.2 Case Study 1: Measuring the Extra Mass Loaded by the Sputtering System

Gold is deposited on a specific device to measure its mass resolution. A well calibrated sputtering system is utilized for this purpose. Au is deposited in four discrete steps to see the repeatability of the experiments and calculate the responsivity constant relating the associated frequency shifts to the extra mass loading. The specific cantilever used for the measurement had a width of 6 μm and a length of 60 μm. Its thickness is measured to be 1.4 μm. In the first session, deposition carried out for 300 seconds leading to an accumulation of 173.0 pg of Au. The associated frequency shift is given in Figure 5.1
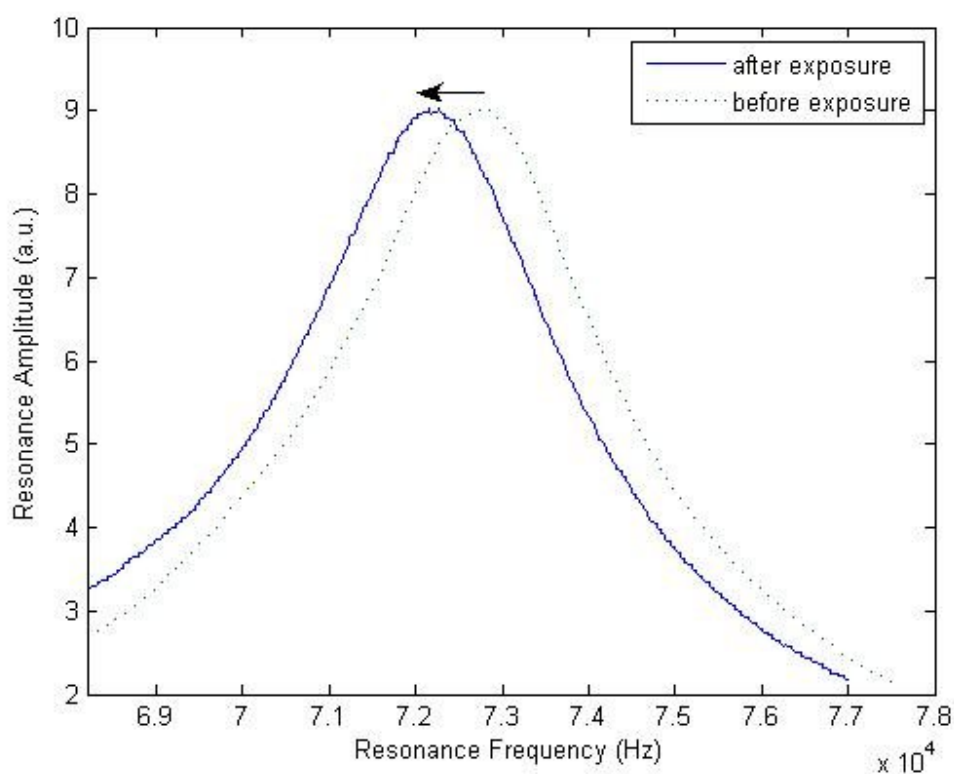
Figure 5.1: Resonance frequency shift due to Au loading

Then, Au deposited for three more discrete steps. In the second trial deposition is carried out leading to an accumulation of 189.0 pg of Au. Corresponding frequency shift is measured. Afterwards, deposition time is reduced for the next two sessions and the measured mass accumulation is found to be 80.0 pg and 102.5 pg. The associated frequency measurements are given in Figure 5.2.
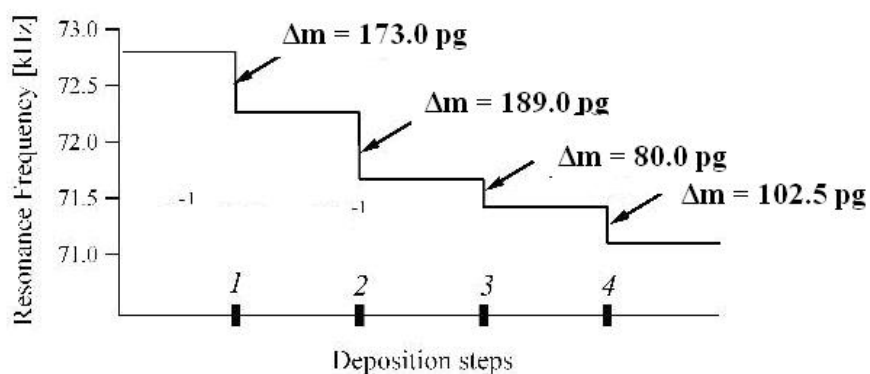
Figure 5.2: The change in the resonance frequency of a cantilever due to a sequence of controlled Au deposition.

The mass responsivity of the specific device is calculated as 0.32 Hz pg^{-1} according to these results. Combined with the already measured RMS error of the frequency measurements this leads to a mass resolution of 0.5 pg at 72 kHz.

5.3 Case Study 2: Functionalization of the Device and Measuring the Mass Accumulation of the Proteins.

Device is functionalized for the bio-sensing experiments. Protein molecules are attached on a cantilever of dimensions 7μm × 70 μm and the resonance frequency shift is measured. The thickness of the cantilever in this case is 1.3 μm. For this purpose the cDNA of human kappa opioid receptor (hKOR) [40] is PCR amplified and cloned into pMAL-c2x vector and named as pNO1. pNO1 is transferred into *E.coli* and hKOR protein is expressed with IPTG for 9 hours at 37°C. The receptor is then purified through Ni-NTA agarose resin. Then it is immobilized on the Au surface of the cantilever via thiol groups of DSP linker through His tag [41]. The shift of 180 Hz shown in Figure 5.3 corresponds to a mass accumulation of 85 pg. This result has a quite consistency with theoretical expectations since the formation of a monolayer of proteins on the cantilever surface is estimated to lead to a mass accumulation of 40 pg. Our measurements indicate that adsorbed proteins exhibit a bilayer structure rather than a monolayer.
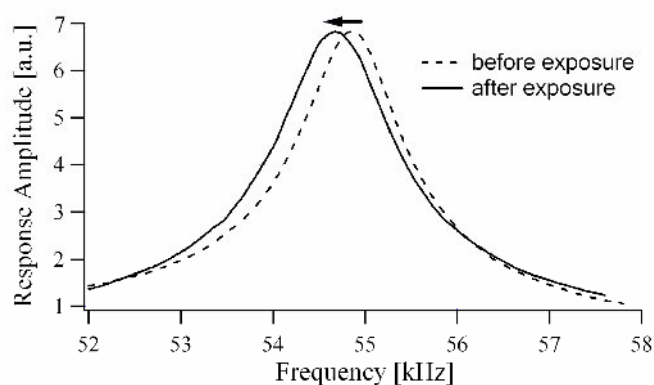
Figure 5.3: Resonance frequency shift of a cantilever due the attachment of human opioid receptors to the Au surface.

5.4 Case Study 3: Studying the anti-body binding

Ability of the device for sensing the bio-molecules is demonstrated however, the device should sense also the corresponding anti-body of the bonded protein to be used as a bio-sensor. For this purpose, a reference chip and a functionalized chip is used. Five cantilevers on each chip are characterized prior to functionalization. Then, thiol groups are formed on cantilevers by reacting 1mM DSP with 10mM Lys-NTA in NaHCO3, pH 8.0 for 3 hours and exposing it to gold surface for 2 hours by gentle shaking. The surface is treated by 50mM NiCl2 for 15 min to allow NTA to capture Ni2+ ions. The protein is allowed to be immobilized on the surface, which is equilibrated previously with solubilization buffer without β-mercaptoethanol, for 1hr with gentle shaking. Then, the surface is blocked by 5% BSA for 1 hr to avoid any non-specific protein binding. Subsequent to the functionalization, resonance frequency shifts of the cantilevers are measured. After measurements has been taken, the sample is treated with anti-his probe, which recognizes 6x Histine tag of the protein, for 1 hr to accumulate further mass on the system. Then, resonance frequency of the cantilevers is measured again. As a reference, another cantilever array is subjected to each processes stated above except for treatment with protein, BSA and anti-his probe. Results are shown in Table 1:

Chapter 5: Case Studies in Mass Detection

	Before Procs (Hz)	After Proc #1 (Hz)	After Proc #2 (Hz)	Shift #1 (Hz)	Shift #2 (Hz)	M#1 (pg)	M#2 (pg)
Reference Chip	121250	120200	120460	-1050	260	86.274	-21.201
	124050	121750	122010	-2300	260	187.518	-20.932
	98700	94470	94570	-4230	100	445.263	-10.279
	113900	109080	109050	-4820	-30	439.285	2.676
Functionalized Chip	193930	189070	188510	-4860	-560	347.842	39.749
	216360	208550	207770	-7810	-780	509.707	50.251
	188600	181950	181660	-6650	-290	497.230	21.346
	186810	179160	178510	-7650	-650	582.663	48.738
	191650	185220	184560	-6430	-660	471.867	47.864

Table 5.1: Frequency shifts in the reference and functionalized chip

  Proc # 1: Binding of human opioid receptors to the the cantilevers

  Proc # 2: Binding of anti-his probe of the receptors to the cantilevers

  M # 1 : Amount of the accumulated mass to the cantilevers during

    Proc #1

  M # 2 : Amount of the accumulated mass to the cantilevers during

    Proc #2

The shift in resonance frequency of cantilevers on each chip indicates mass accumulation or mass loss. The resonance frequency shift at reference chip is very significant after first process. This significant shift shows that glycerol in treatment buffer

is accumulated on the chip. The high deviation at accumulated mass reveals that the glycerol distribution over cantilevers is nonuniform. Although mass accumulation at the reference chip is very high and diverse, it becomes higher at each cantilever of protein immobilized chip. Since glycerol in treatment buffer is also accumulated on this chip, it can be asserted that protein immobilization is accomplished and mass accumulatation is detected successfully. After second process, mass loss is observed at the reference chip. This loss can be identified with successful removal of residual glycerol on the chip. Before proceeding to second process, drying the chip under N_2 has enabled cantilevers to be cleaned effectively. Hence, the accumulated mass on protein immobilized chip is the mass of antibodies, which simply recognize only immobilized proteins. Additionally, the measured mass is very close to expected antibody mass. Figure 5.4 reveals the mean resonance frequency shifts due to protein and anti-body binding.
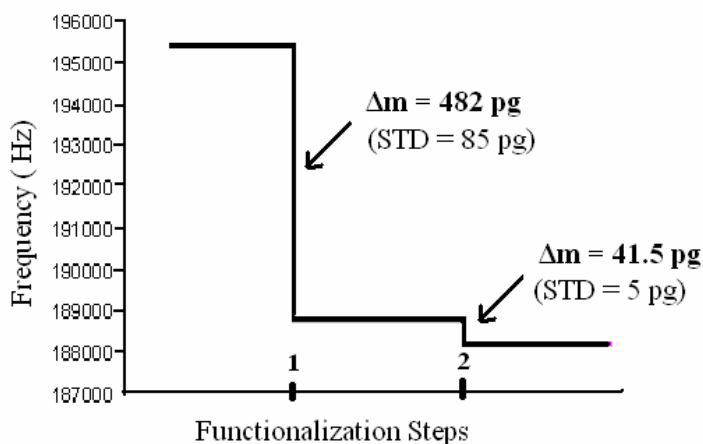
Figure 5.4: Mean deviation in the resonance frequency of the cantilevers during Proc # 1 and Proc # 2

By those three case studies, utilization of the device for both inorganic and organic mass sensing is demonstrated. Thereafter, operation principles and the intrinsic properties of the device are investigated. Stress on the cantilevers due to electroplating is analyzed. Operation of the device in water is tested and effect of a DC coupling to the magnetic actuation is observed. Output of the PD signal for different diffraction orders and cantilevers are investigated. Finally, reliability of the FEM numerical analysis is studied.

Chapter 6

Discussion

6.1 Stress accumulated by Ni electroplating

According to results of the FEM analysis which will be explained in the forthcoming sections, resonance frequency of a cantilever beam has a major dependency on residual/intrinsic stresses. For stress anaylsis, curvatures of the wafers are measured since the relation between the stress and the radius of curvature is provided by the Stoney formula [42]:

$$\sigma = \frac{1}{6}\left(\frac{1}{R_{post}} - \frac{1}{R_{pre}}\right)\frac{E}{(1-\nu)}\frac{t^2_{s}}{t_f} \qquad (6.1)$$

where σ is the stress, R_{post} and R_{pre} are the radius of curvatures after and before the deposition, t_s and t_f are the substrate and film thicknesses, ν and E are the Poisson ratio and the Young Modulus of the deposited film respectively.

Firstly, the curvature of the Silicon wafer is measured over a 5 centimeter long path with a DEKTAK 8.1 profiler. Afterwards, gold is sputtered on the wafer and curvature is measured along the same line. Finally, whole wafer is electroplated with Nickel and the final curvature is measured. The result is provided in Figure 6.1
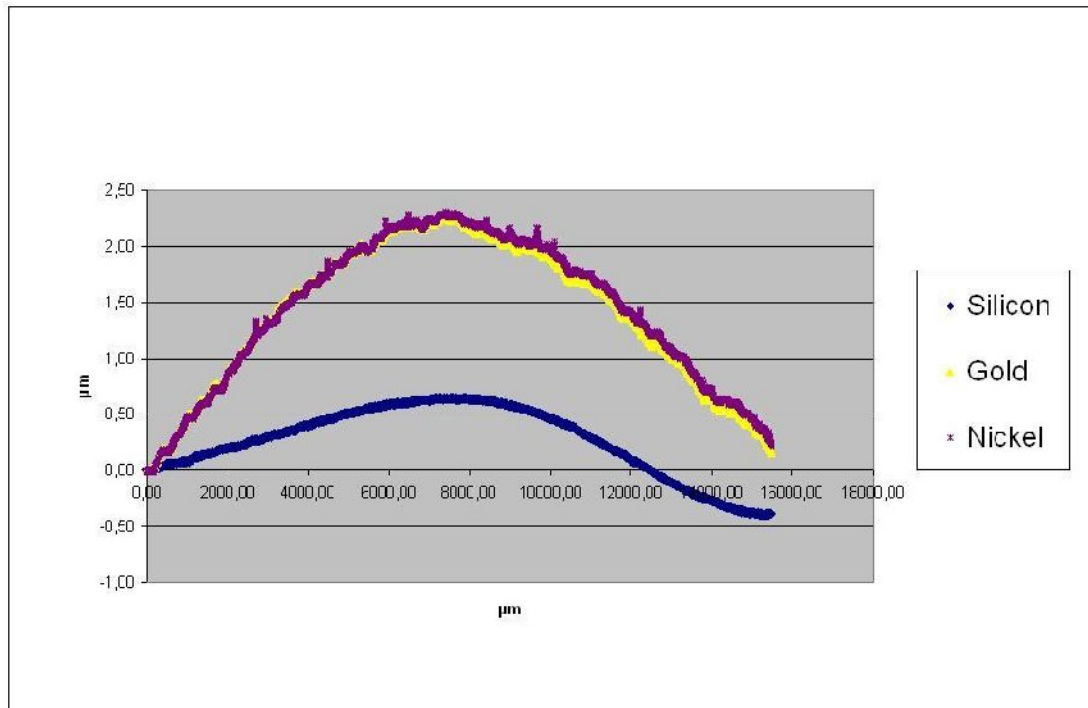
Figure 6.1: Deflection measurements along the wafer

Horizontal axis of Figure 6.1 represents the line along which the measurement is done and vertical axis represents the deflection of the wafer. Using this data, radius of curvatures is calculated. Radius of the curvature before and after the electroplating step is found same. So, according to equation 6.1, it can be concluded that no stress is caused by the electroplating step. However, deposition of gold changed the magnitude of the curvature and caused stress on the wafer. So, Au is deposited onto wafer via different processes to reduce the extra curvature caused by gold.

Three different experiments are done to see the stress effect of different depositions. Three Si wafers are used. Curvatures of all wafers are measured before the experiments. In the first experiment, Au is deposited onto Si wafer by sputtering at ambient temperature. Deposition of Au is carried via sputtering at 250° C for the second experiment. Finally,

gold is evaporated onto the silicon surface to compare the curvature caused by gold with the sputtering experiments. Results are shown in Figure 6.2.
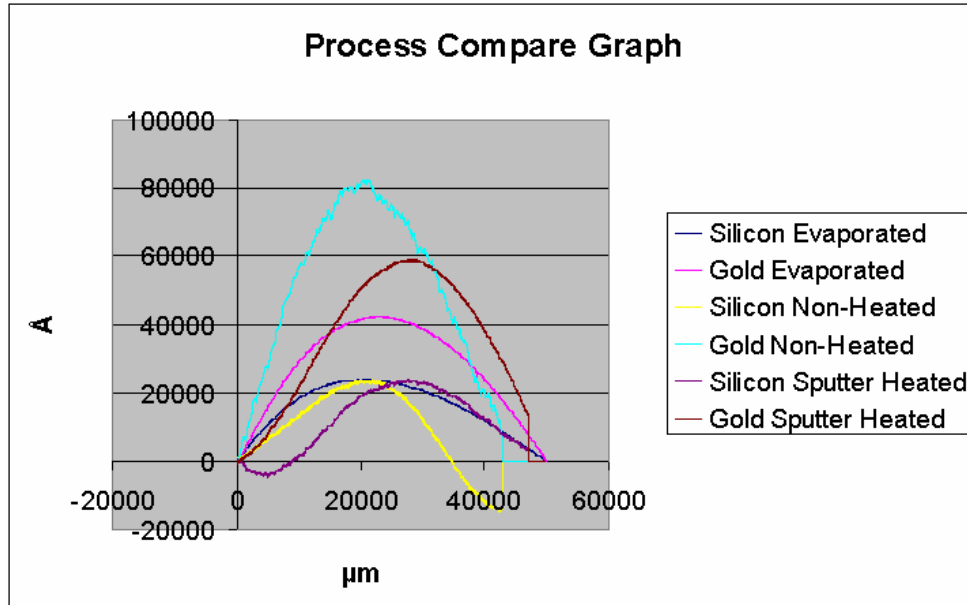
Figure 6.2: Deflection measurements for different processes of deposition

Figure 6.2 represents the deflection measurements before and after the deposition of Au. Three curves whose maximum are at the level of 20000 Angstroms represent the curvature measurements before the deposition of Au and labeled as "Silicon-Deposition type" at the legend. The other three curves represent the curvatures after the deposition of Au and labeled as "Gold-Deposition Type". As represented in the figure, there is a slight difference of curvatures for different deposition procedures. It is identified that curvature change is minimum via the evaporation process of Au. So, the stress accumulated by deposition of gold is minimal according to equation 6.1. Although processing the sputtering experiment at high temperatures causes more stress than evaporation, it seems to give a better result than the sputtering at ambient temperature. It can not be concluded surely

which procedure is best to reduce the stress via making single experiments for each procedure. However, it can be concluded that there is not a big difference of the curvatures for different processes of deposition of Au.

6.2 Operation in Liquid Media

One of the major purposes of this study is to propose a device which operates in liquid since operation in liquid is a necessity for the device to be used as a biosensor. Hence, operation of the device in water is tested. Same experimental setup is used and procedure is followed for operation in water. Thanks to magnetic actuation the device could be operated in liquid media by means of a small water reservoir. Device is placed into water and electromagnetic coil is placed behind the cup. Hence, device is actuated in water and the behavior of the device in water is observed. Operation of the same cantilever in air and water is observed for this purpose. Width and length of the cantilever is 5 μm and 25 μm, respectively. Thickness is 0.95 μm. Resonance behaviors of the device in air and water are shown in Figure 6.3.
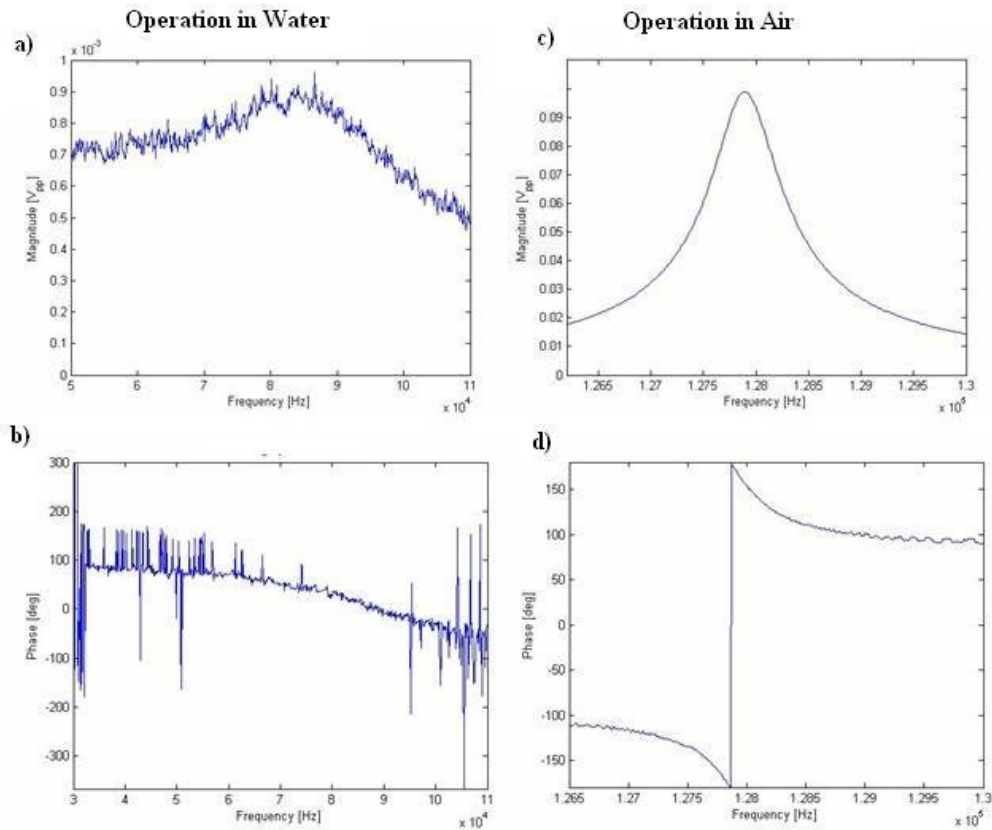
Figure 6.3: Comparison of the resonance behavior of a device in air and water

a) Resonance Curve in water. b) Phase shift in water. c) Resonance curve in air.

d) Phase shift in air

Quality factor of the cantilever is on the order of 10^2 in air. However, it tremendously decreased in water to the order of 10^0. Resonance frequency is 127880 Hz in air where it is found to be 86600 Hz in water. The sharp phase shift at resonance also yielded a slow and continuous transition in water. Resonance frequency decreases by

nearly a factor of 2/3 in water. This experiment demonstrated the ability of device operation in liquid media. On the other hand, Q factor of the cantilever in liquid media can be increased up to three orders of magnitude via positive feedback [43]. Equation of motion for a damped system is given by equation 6.2;

$$F = m\ddot{x} + b\dot{x} + kx \qquad (6.2)$$

where b is the damping coefficient of the media. By a feedback control if an additional term is added to external force which is proportional to velocity (i.e. $c\dot{x}$), then the effective damping coefficient drops (*b-c)* which increases the quality factor.

Water experiment is repeated for a second cantilever to compare the result with the previous one. Cantilever used for this purpose had a width of 5 µm and length of 25 µm. Thickness is measured as 0.90 µm. Results are shown in Figure 6.4
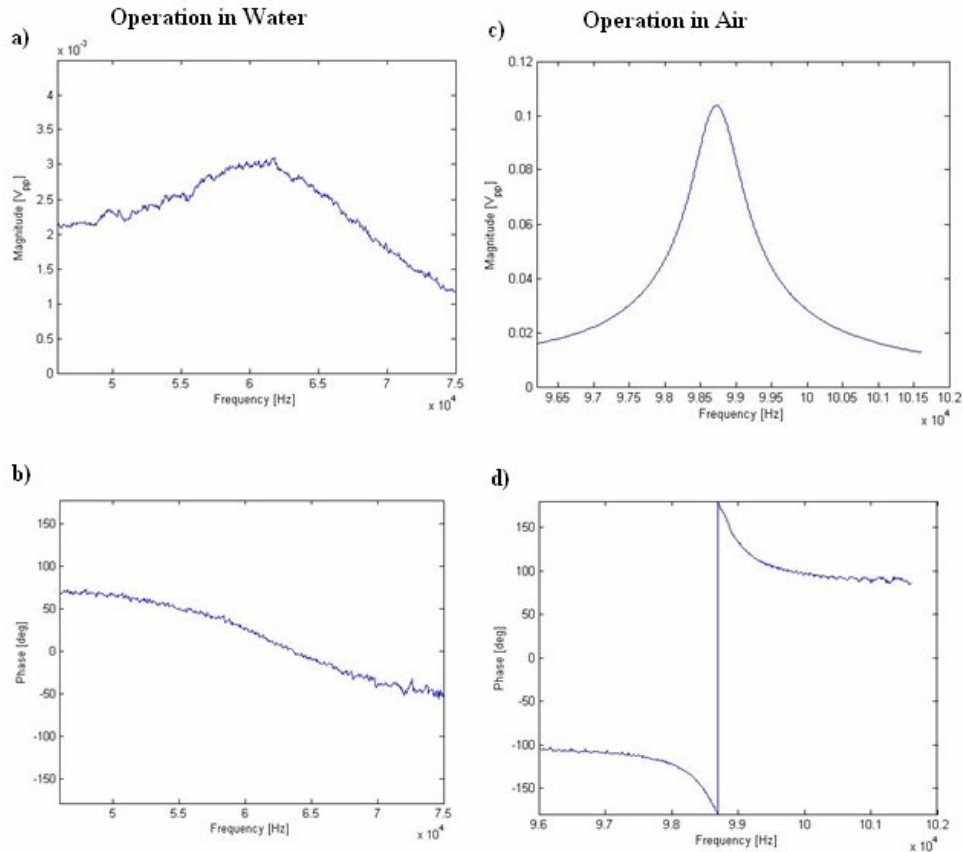
Figure 6.4: Comparison of the resonance behavior of a device in air and water

b) Resonance Curve in water. b) Phase shift in water. c) Resonance curve in air.

d) Phase shift in air

Same resonant behavior is observed with the previous experiment. Q factor of the device again tremendously decreased to order of 10^0 and the resonance frequency is decreased by a factor of 2/3.

Also the effect of DC coupling in water is investigated. Because when a magnet is brought close to cantilever, the DC field of the magnet causes a coupling of the force on the

cantilever and this increases the resonance amplitude and decreases the noise level. For this purpose, a cantilever having 11 µm width and 55 µm length is used. Thickness of the cantilever is measured as 1.2 µm. A big magnet is brought closer to the structure and water experiment is repeated. Result is shown in Figure 6.5
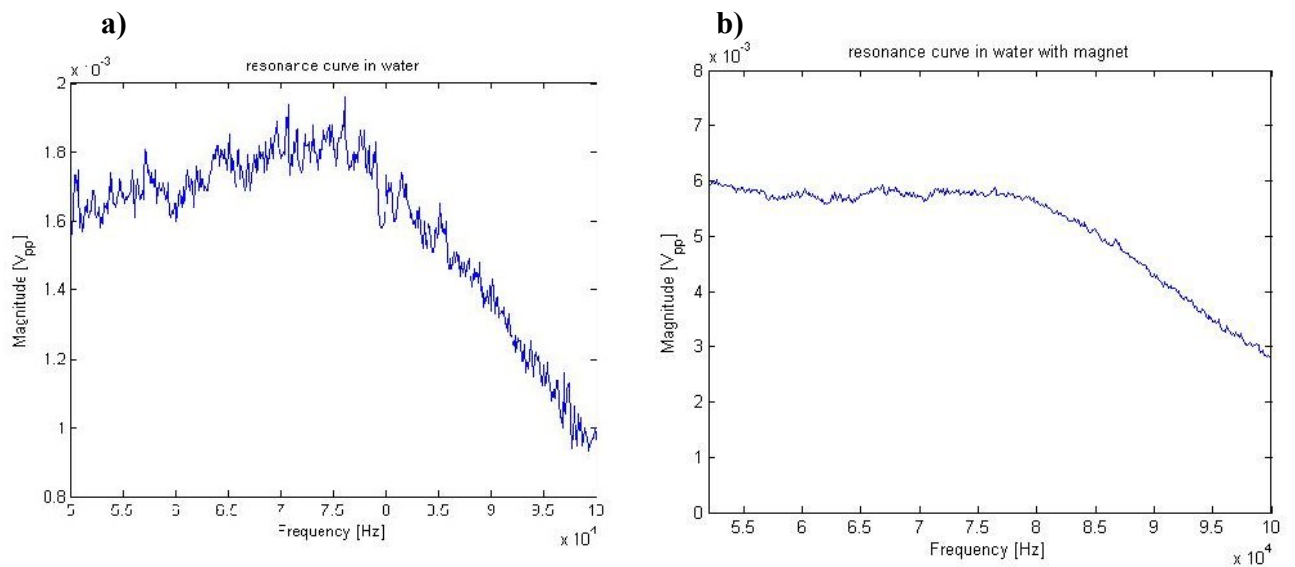
Figure 6.5: Comparison of the behavior in water with and without a magnet.

Graphs show that the magnet did not have a positive affect on the Q factor of the cantilever. Also the resonance frequency did not change.

6.3 Remarks Concerning Photodiode Output

As explained in the third chapter, 0th or 1st order of the diffracted light is focused onto the photodiode to observe the intensity modulation while the cantilever oscillates. Since cantilever displacements are very small especially at high frequencies, intensity

modulation is small too. Especially peak-to-peak voltages for the 1st order of the diffracted light can be in the order of a few millivolts. Noise becomes very significant at such small values and 0th order of the diffracted light is used for the measurement of the intensity modulation mostly due to its higher voltage output.

Intensity modulates with a period of $\lambda/2$ with respect to the gap between the gratings and the fixed surface as shown in Figure 6.6. Sinusoidal change of intensity has one maximum and one minimum point in a period of $\lambda/2$. Hence, if a cantilever oscillates in a way that it passes the maximum or minimum intensity twice, that causes a cut-off in its sinusoidal modulation. Photodiode output of a such behavior is presented in Figure 6.7:
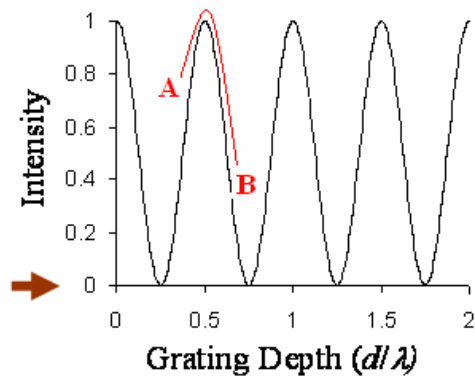
Figure 6.6: Cantilever oscillates between the points A and B and passes the maximum intensity point twice.

Chapter 6: Discussion
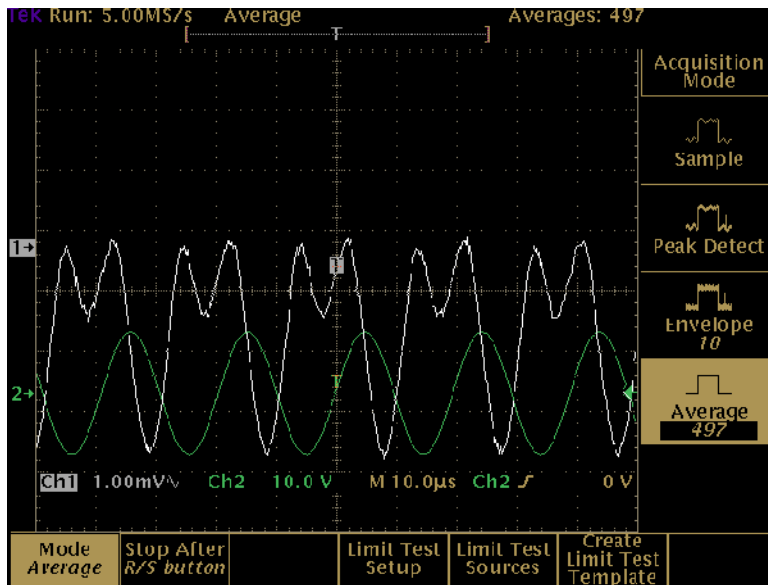
Figure 6.7: Intensity modulation of the 1st order diffracted light

One important remark about the optic readout is that the position of the photodiode and the sample is very important during the measurements. Diffracted light should be focused onto the PD very properly that the other reflections from the sample surface should be avoided to get a signal with high SNR ratio. Laser beam should also be focused just onto gratings that the interference pattern seems clear.

6.4 Finite Element Analysis of the Results

Aim of finite element studies is to obtain a relation between the mass increments and the related frequency drop. Experimental frequency data are used to model the mass increments. Mass increments are simulated by increasing the density of the structures. The initial density is driven as 8908 kg/m^3, density of Nickel. Poisson ratio of Nickel is 0.31 and it has a elastic modulus of 205 GPa. However, a modulus of 124 GPa is used in

Chapter 6: Discussion

simulations since it gave agreeable results with the experimental results. Modulus of the Ni is mostly determined by the fabrication of the structures. Modulus value has a dependency on the fabrication temperature.

Simulations are made in ANSYS by arranging the thickness of the structures in such a way that the model has the same frequency with the experimental measured frequency. Then, effects of mass increments to the resonance frequencies are studied. Figure 6.7 shows the meshed model of a cantilever designed by means of ANSYS:
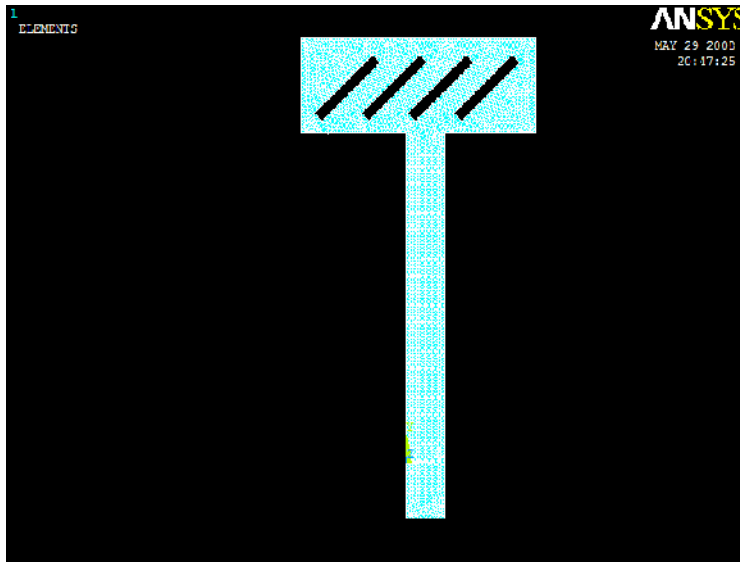
Figure 6.8: ANSYS model of a cantilever beam

Cantilever having a width of 6 µm and length of 60 µm is simulated by ANSYS whose frequency changes are measured experimentally due to mass increments. Thickness of the cantilever is measured as 1.4 µm. Modulus, Poisson ratio and density of the Nickel are the other fit parameters that are used as the input of the simulation. Results are provided in Table 6.1:

Chapter 6: Discussion

Frequency (Hz)	Mass (picogram)	ΔF (Hz)	Δm (picogram)	ΔF/ Δm (Hz/Pg)
72828	11224	-	-	
72259	11402	-569	+178	3.196
71671	11589	-588	+187	3.144
71423	11670	-248	+81	3.061
71101	11776	-322	+106	3.037

Table 6.1: Relation between the resonance frequency and the mass increment

The relation between the mass increment and frequency decrease is analyzed by this simulation. The ratio of frequency decrease to mass increment (ΔF/Δm) is calculated as approximately 3 which means that the resonance frequency decreased 3 Hz for added each picogram of mass. It is obvious that ΔF/ Δm is not same for all the experiments. Initially one picogram of mass caused a shift of 3.196 Hz but as more mass is added, one picogram is able to shift 3.144 Hz, 3.061 Hz and 3.037 Hz respectively. Change in the ΔF/ Δm through the mass increment process exposes that very small amounts of masses compared to the mass of the cantilever should be added to calculate the responsivity constant. If not, there occurs a nonlinear behavior between the mass increment and change in the resonance frequency.

For further analysis of the relation between the mass increment and the shift in resonance frequency, a structure having a width of 7 µm and length of 70 µm is simulated. Experimentally measured resonance frequency of the structure is 54850 Hz and the thickness of the device is arranged as 1.29515 microns to adjust the frequency of the

Chapter 6: Discussion

ANSYS model to the experimentally measured value. Then, extra mass is loaded onto the device and corresponding frequency shift is measured. Result is shown in Table 6.2

Frequency	Mass	ΔF	Δm	ΔF/Δm
54850 Hz	12850 picogram	-	-	
54669 Hz	12935 picogram	-181 Hz	+85 picogram	2.13

Table 6.2: Relation between the mass increment and resonance frequency (width = 7 μm, L = 70 μm)

When results are compared to the previous simulation, it is very important to notice that ΔF/Δm value significantly changed.   Results exhibit that the resonance frequency of a cantilever should be modeled very properly to obtain a clear picture of the relation between ΔF and Δm.

Thickness dependence of the resonance frequency is also studied. Resulting graph is shown in Figure 6.8:
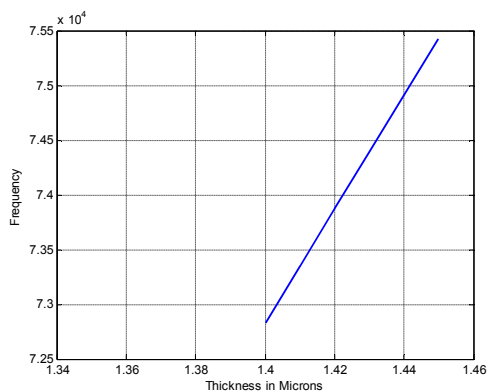
Figure 6.9: Relation between the thickness and frequency.

Chapter 6: Discussion

Linear relation is found between the thickness and resonance frequency. Length and width of the studied structure are 70 μm and 7 μm respectively. It is seen that 10 nm increase in the thickness caused 520 Hz increase in the frequency.

Finally, relation between the stress on the cantilevers and resonance frequency is analyzed. Results are presented in Table 6.3

Case Number	Applied Von Mises Stress (MPa)	Frequency (Hz)	Δf (Hz)	Applied Stress (Hz / MPa)
Initial	-	498.55	-	-
Case 1	83.3	731.23	232.68	2.793
Case 2	139	848.38	349.83	2.516
Case 3	222	995.9	497.35	2.240
Case 4	278	1081.9	583.35	2.098

Table 6.3: Shift in the resonance frequency due to the applied stress.

The effect of stress on frequency is observed in this simulation significantly. The ratio between the frequency shifts vs. applied stress is approximately 2, varying with the total stress applied on the model, as seen in the table above.

Chapter 6: Discussion

To conclude the results, non-linear relation between the mass increment and frequency is obtained. Hence, it is very important to simulate the resonance frequency of the beam properly to calculate the corresponding mass increment.

Chapter 7

Conclusion and Future Work

In summary, micron-sized Nickel cantilevers with integrated diffraction gratings are fabricated to be used as highly sensitive mass sensors. Dynamic mode of operation is utilized to sense the amount of the accreted species onto devices. Shift in the resonance frequency of the devices are measured by means of a photodiode setup utilizing grating interferometry principles. Fabrication of the structures is carried out via micro-machining methods. UV photolithography is used as the patterning method. Cantilevers are actuated magnetically to be driven at their resonance modes. Thanks to the noise rejection capability of AC detection and the simple grating readout principle, the signal-to-noise ratio of the optical readout method is shown to be comparable to that of LDV measurements. Characterization of several structures is carried out and effect of the geometry of the structures to their resonance frequencies is explored. Two case studies utilizing the cantilevers as mass sensors are performed. Both the organic and inorganic mass sensing properties and the potential utilization of the devices as biosensors are demonstrated. Operation principles of the devices are investigated. Stress accumulated onto structures during electroplating step is studied and operation of the devices in liquid media is demonstrated. Operation of the devices is modeled via Finite Element Numerical Analysis to measure the amount of the loaded mass.

There are two important processes which have been and should be studied regarding the device operation. First one is improving the Quality Factor (Q) of the device for

operation in liquid (Q ~ 1) since the device actually will be operated in liquid media for bio-sensing. Motivation behind increasing Q is that AC detection requires a high Quality Factor for obtaining a precise value for the frequency shift. Second one is Self-oscillation for operating the device at it's resonance without providing any AC signal to the device.

In literature, a novel technique that increases the quality factor of the cantilever in a liquid up to three orders of magnitude via positive feedback [43]. The positive feedback loop monitors the cantilever response and shift it 90° and amplify it with a gain G, to produce a second input signal that is proportional to velocity of the cantilever which decreases the effective damping coefficient.

Second technique is tracking the resonance frequency by amplifying the Brownian noise [44]. To amplify the Brownian amplitude signal from the PD, it is fed to a variable gain amplifier and a variable phase shifter and feeding it back to cantilever. If the phase of the feedback signal is adjusted to have 90° phase lag to the output signal of the PD, Brownian motion of the cantilevers will be amplified and they will oscillate at resonance.

Parallel array readout and improvement of the fabrication process are the further developments regarding the device operation. If the laser beam is focused on several cantilevers and the output is collected on the same photodiode, resonance frequency of all the cantilevers can be tracked by a single output. Intensity of the output signal is mostly dependent on the smoothness of the sample. There are two important steps during the fabrication process that affects the roughness of the sample surface: i) the electroplating step affecting the shine of the nickel, ii) etching of Silicon to release the structures. Electroplating temperature, duration and current density are the three parameters of this step which can be further investigated to obtain a shinier Ni surface. On the other hand, in literature some studies report that mixing the KOH solution with Isopropyl Alcohol at certain percentages may improve the roughness of the Si surface after etching [45]. Noise

analysis is also an important part of the process that should be carried out profoundly to set the minimum detectable mass of the device.

Operation of the device for bio-sensing is demonstrated. Furthermore, selectivity of the device to different biological species should be studied for the potential usage as a biosensor.

BIBLIOGRAPHY

1. H. G. Craighead, Nanoelectromecahnical Systems, Science, 290 (2000),1532-1535.

2. B. Ilic, H. G. Craighead, S. Krylov, W. Senaratne, C. Ober, P. Neuzil, Attogram detection using nanoelectromechanical oscillators, Journal of Applied Physics, 95 (2004), 3694-3703.

3. H. P. Lang, M.K. Baller, R. Berger, Ch. Gerber, , J.K. Gimzewski, F.M. Battiston, P. Fornaro, .P. Ramseyer, E. Meyer, Güntherodt, An artificial nose based on a micromechanical cantilever array, Analytica Chimica Acta, 393 (1999), 59-65.

4. Y. T. Yang, C. Callegari, X. L. Feng, K. L. Ekinci, and M. L. Roukes, Zeptogram-Scale Nanomechanical Mass Sensing, Nano Letters, 6 (2006), 583-586.

5. Christiane Ziegler, Cantilever-based Biosensors, Analytical Bioanalytical Chemistry 379 (2004), 946-959.

6. M. K. Baller, H.P. Lang, J. Fritz, Ch. Gerber, J.K. Gimzewski, U. Drechsler, H. Rothuizen, M. Despont, P. Vettiger, F.M. Battiston, J.P. Ramseyer, P. Fornaro, E. Meyer, H. J. Güntherodt, A cantilever array-based artificial nose, Ultramicroscopy, 82 (2000), 1-9.

7. A. Gupta, D. Akin, and R. Bashir, Single virus particle mass detection using microresonators with nanoscale thickness, Applied Physics Letters, 84 (2004), 1976-1978.

8. B. Ilic, D. Czaplewski, M. Zalalutdinov, H.G. Craighead, P. Neuzil, C. Campagnolo, C. Batt, Single cell detection with micromechanical oscillators, Journal of Vacuum Science Technology B, 19 (2001), 2825-2828.

9. D. Ramos, J. Tamayo, J. Mertens, and M. Calleja, Origin of the response of nanomechanical resonators to bacteria adsorption, Journal Applied Physics 100 (2006), 106105.

10. B. Ilic, Y. Yang, K. Aubin, R. Reichenbach, S. Krylov, H. G. Craighead, Enumeration of DNA Molecules Bound to a Nanomechanical Oscillator, Nano Letters, 5 (2005), 925-929.

11. F. M. Battison, J. P. Ramseyer, H. P. Lang, M. K. Baller, Ch. Gerber, J. K. Gimzewski, E. Meyer, H.-J. Güntherodt, Sensors and Actuators B, 77 (2001), 122-131.

12. Dazhong Jin and Xinxin Li, Hanhan Bao, Zhixiang Zhang, Yuelin Wang, Haitao Yu, and Guomin Zuo, Integrated cantilever sensors with a torsional resonance mode for ultraresoluble on-the-spot bio/chemical detection, Applied Physics Letters, 90 (2007), 041901

13. K. K. Park, H. J. Lee, G. G. Yaralioglu, A. S. Ergun, Ö. Oralkan, M. Kupnik, C. F. Quate, and B. T. Khuri-Yakub, T. Braun, J.-P. Ramseyer, H. P. Lang, M. Hegner, and Ch. Gerber, J. K. Gimzewski, Capacitive micromachined ultrasonic transducers for chemical detection in nitrogen, Applied Physics Letters, 91 (2007), 094102

14. T. Adrega and V. Chu, J. P. Conde, Resonance of electrostatically actuated thin-film amorphous silicon microelectromechanical systems microresonators in aqueous solutions: Effect of solution conductivity and viscosity, Journal of Applied Physics, 101 (2007), 094308

15. Amit Gupta and Demir Akin, Rashid Bashir, Detection of bacterial cells and antibodies using surface micromachined thin silicon cantilever resonators, Journal of Vacuum Science and Technology B, 22 (2004), 2785-2791

16. Z.J. Davis, G. Abadal, B. Helbo, O. Hansen, F. Campabadal, F. Pérez-Murano, J. Esteve, E. Figueras, J. Verd, N. Barniol, A. Boisen, Monolithic integration of mass sensing nano-cantilevers with CMOS circuitry, Sensors and Actuators A, 105 (2003), 311-319

17. K. K. Park, H. J. Lee, G. G. Yaralioglu, A. S. Ergun, Ö. Oralkan, M. Kupnik, C. F. Quate, and B. T. Khuri-Yakub, T. Braun, J.-P. Ramseyer, H. P. Lang, M. Hegner, and Ch. Gerber, J. K. Gimzewski, Capacitive micromachined ultrasonic transducers for chemical detection in nitrogen, Applied Physics Letters, 91 (2007), 094102

18. Nickolay V. Lavrik, Michael J. Sepaniak, Panos G. Datskos, Cantilever transducers as a platform for chemical and biological sensors, Review of Scientific Instruments, 75 (2004), 2229-2253

19. C. A. Savran, T. P. Burg, J. Fritz, and S. R. Manalis, Microfabricated mechanical biosensor with inherently differential readout, Applied Physics Letters, 83 (2003), 1659-1661

20. Christopher Palmer, Diffraction Grating Handbook, Richardson Grating Laboratory, 2002

21. Carl G. Chen and Mark L. Schattenburg, A Brief History of Gratings and the Making of the MIT Nanoruler, 2004

22. Caglar Ataman, Hakan Urey and AlexanderWolter, A Fourier transform spectrometer using resonant vertical comb actuators, J. Micromech. Microeng. 16 (2006) 2517–2523

23. Alexander Bunkowski, Ms Thesis, Leibniz Universit¨at Hannover, 1976

24. O. Manzardo, H. P. Herzig, C. R. Marxer, and N. F.de Rooij, Miniature lamellar grating interferometer based on silicon technology, Opt. Lett. 24, 1705 (1999).

25. J. Strong and G. A. Vanasse, J. Opt. Soc. Am. 50, 113 (1960)

26. Caglar Ataman, Hakan Urey and AlexanderWolter, A Fourier transform spectrometer using resonant vertical comb actuators, J. Micromech. Microeng. 16 (2006) 2517–2523

27. Luke Johnson, Amit K. Gupta, Azam Ghafoor, Demir Akin, Rashid Bashir, Characterization of vaccinia virus particles using microscale silicon cantilever resonators and atomic force microscopy, Sensors and Actuators B, 115 (2006), 189-197.

28. Neal A. Hall and F. Levent Degertekin, Integrated optical interferometric detection method for micromachined capacitive acoustic transducers, 20(2002), 3859-3861

29. 10. A. M. Moulin, S. J. O'Shea, R. A. Badley, P. Doyle, and M. E. Welland, Langmuir, 15 (1999), 8776 -8779

30. Takahito Ono, Xinxin Li, Hidetoshi Miyashita, Masayoshi Esashi, Mass sensing of adsorbed molecules in sub-picogram sample with ultrathin silicon resonator, Review of Scientific Instruments, 74 (2003), 1240-1243

31. M. L. Roukes, Nanoelectromechanical Systems: Potential, Progress, & Projections, IEEE MEMS 2007, (2007), 93-94

32. K. L. Ekinci, Y. T. Yang and M. L. Roukes, Ultimate limits to inertial mass sensing based upon nanoelectromechanical systems, Journal of Applied Physics, 95 (2004), 2682-2689

33. R. B. Darling / EE-527

34. J.K. Luo, A.J. Flewitt, S.M. Spearing, N.A. Fleck, W.I. Milne, Young's modulus of electroplated Ni thin film for MEMS applications, Materials Letters, 58 (2004), 2306- 2309.

35. J.K. Luo, A.J. Flewitt, S.M. Spearing, N.A. Fleck, W.I. Milne, Young's modulus of electroplated Ni thin film for MEMS applications, Materials Letters, 58 (2004), 2306-2309

36. Mimiwaty Mohd Noor, Badariah Bais, and Burhanuddin Yeop Majlis, The Effects Of Temperature and KOH Concentration on Silicon Etching Rate and Membrane Surface Roughness, IEEE ICSE 2002, (2002), 524-528.

37. S. O. Isikman, O. Ergeneman, A. D. Yalcinkaya, and H. Urey, Modeling and Characterization of Soft Magnetic Film Actuated 2-D Scanners IEEE Journal of Selected Topics in Quantum Electronics 12, 283 (2007).

38. O. Ferhanoglu, M. F. Toy, and H. Urey, IEEE Photonics Technology Letters 19, 1895 (2007).

39. F.R.Blom,S.Bouwstra, M. Elwenspoek, J.H.J. Fluitman, J.Vac.Sci.Technology B, 10(1992), 1

40. F. Simonin, C. Gavériaux-Ruff, K. Befort, H. Matthes, B. Lannes, G. Micheletti, M.-G. Mattéi, G. Charron, B. Bloch, and B. Kieffer, κ-Opioid receptor in humans: cDNA and genomic cloning, chromosomal assignment, functional expression, pharmacology, and expression pattern in the central nervous system, The Proceedings of the National Academy of Sciences Online USA, 92 (1995),7006-7010.

41. S. A. Trammell, L. Wang, J. M. Zullo, R. Shashidhar, and N. Lebedev, Orientated

binding of photosynthetic reaction centers on gold using Ni-NTS self-assembled monolayers, Biosensors and Bioelectronics, 19 (2004), 1649-1655

42. A. M. Moulin, S. J. O'Shea, R. A. Badley, P. Doyle, and M. E. Welland, Langmuir, 15 (26), 8776 -8779, 1999

43. J. Tamayo, A.D.L. Humphris, A.M. Malloy, M.J. Miles, Ultramicroscopy 86 (2001) 167-173

44. Adosh Mehta, Suman Cherian, David Hedden, Thomas Thundat, Applied Physics Letters, 78, 11 (2001)

45. Mimiwaty Mohd Noor, Badariah Bais, and Burhanuddin Yeop Majlis, The Effects of Temperature and KOH Concentration on Silicon Etching Rate and Membrane Surface Roughness, IEEE ICSE 2002, (2002), 524-528

VITA

Alibey Öztürk was born in Konya, Turkey on 1982. He graduated from Konya Meram Science High School in 2000. He had his undergraduate studies in Bilkent University, Ankara, Turkey under full scholarship where he held his B.S. degree on physics. After graduation, in 2006, he was accepted from Materials Science and Engineering Department of Koç University, Istanbul, Turkey for graduate studies. During his M. Sc. Studies he worked on *biosensor applications of Microelectromechanical Systems (MEMS) with integrated optical readout* under the supervision of Professor B. Erdem Alaca. His main interests of research are micro/nano-fabrication, MEMs/NEMs, bioMEMs and physics of nanoelectronics..

Following his M. Sc. studies he is going to pursue a Ph. D. degree on Physics in Technische Universiteit Delft.